

Robust Data-Driven 3-D Shape Servoing of Unmodeled Continuum Robots Using FBG Sensors in Unstructured Environments

Yiang Lu, Wei Chen, Bo Lu, Jianshu Zhou, Zhi Chen, Qi Dou, and Yun-Hui Liu, *Fellow, IEEE*

Abstract—In this paper, we present a novel and generic data-driven method to servo-control the 3-D shape of continuum robots embedded with fiber Bragg grating (FBG) sensors. Developments of 3-D shape perception and control technologies are crucial for continuum robots to perform the tasks autonomously in surgical interventions. However, owing to the nonlinear properties of continuum robots, one main difficulty lies in the modeling of them, especially for soft robots with variable stiffness. To address this problem, we propose a new robust adaptive controller by leveraging FBG shape feedback and neural networks (NNs) that can online estimate the unknown model of continuum robot and accounts for unexpected disturbances together with NN approximation errors, which exhibits an adaptive behavior to the unmodeled system without priori data exploration. Based on a new composite adaptation algorithm, the asymptotic convergences of the closed-loop system with NNs learning parameters have been proven by Lyapunov theory. To validate the proposed method, we present a comprehensive experimental study by using two continuum robots both integrated with multi-core FBGs, including a robotic-assisted colonoscope and multi-section extensible soft manipulators. The results demonstrate the feasibility, adaptability, and superiority of our controller in various unstructured environments as well as phantom experiments.

Index Terms—Continuum robots, fiber Bragg grating (FBG) sensors, adaptive control, neural networks, shape control.

I. INTRODUCTION

CONTINUUM robots are composed of more compliant materials and flexible structures than traditional rigid-link manipulators, endowing them with high dexterity and compliance for a wide variety of application scenarios, such as industrial fields, human-robot interactions, and medical interventions. In view of the advantages of continuum robots in terms of manipulating accessibility, intraoperative maneuverability, and inherent safety, they possess great potentials to be applied in the treatment of various types of minimally invasive surgery (MIS) [1], such as percutaneous intracardiac surgery [2], laryngeal microsurgery [3], and abdominal interventions

[4]. However, the interference of nonlinear structural characteristics and unknown environmental disturbances would negatively affect the priori modeling of the continuum robots, hence accurate 3-D shape sensing and robust control are considered as major challenges for their efficient and safe implementations in unstructured surgical scenarios [5]–[7] (as illustrated in Fig. 1), such as osteolytic lesion treatment [8] and laser-based tumor ablation [9], especially for soft robotic manipulators integrated with soft materials and structures that exhibit heterogeneous and variable stiffness.

A. Related Work

Considering that continuum robot has an infinite number of degree-of-freedom (DOFs) in configuration space [1], [7], [10], real-time perception of its 3-D shape is essential to advance control strategies. To date, numerous types of sensing modalities have been exploited for shape sensing and position estimation of continuum robots in MIS [6], such as mechanics-based methods [11], intraoperative imaging modalities [12], magnetic resonance imaging (MRI) [13], and electromagnetic (EM) tracking [14]. However, these methods suffer from their limitations concerning acquisition frequency, sensing accuracy, application versatility, and clinical compatibility. Recently, fiber Bragg grating (FBG) sensors have shown great potentials in shape sensing of continuum robots and flexible instruments [15]–[17] due to their lightweight, high compatibility, and high feedback frequency without requiring line-of-sight. Considering severe signal noises of FBG measurements in unstructured environments, the accumulative error along the longitudinal direction could defect the robustness and accuracy of the sensing result. Aiming to solve this problem, some sensor fusion [18], [19] and learning-based approaches [20], [21] have been developed. A model-based filtering algorithm for 3-D shape reconstruction using multi-core FBGs is recently reported to be accurate and robust against the sensory noises and unexpected perturbations [22].

Employing task-space position/shape together with encoders information as feedback, various control methodologies of continuum robots have been proposed for distal endpoint positioning and shape servoing [23], [24]. According to modeling approaches, these control strategies can be mainly classified into model-based and model-free methods. Model-based methods require a priori accurate modeling of the continuum robot, including kinematics/statics and dynamics models [5] based on certain assumptions and theories, e.g., constant/variable curvature [10], [25], [26], beam theory [27], [28], and Cosserat

This work was supported in part of the HK RGC under T42-409/18-R and 14202918, in part by the Shenzhen-HK Collaborative Development Zone, in part by the Hong Kong Centre for Logistics Robotics, in part by the Multi-Scale Medical Robotics Centre, InnoHK, and in part by the VC Fund 4930745 of the T Stone Robotics Institute. (*Corresponding author: Jianshu Zhou and Bo Lu.*)

Y. Lu, W. Chen, B. Lu, J. Zhou, Z. Chen, and Y.-H. Liu are with T Stone Robotics Institute, Department of Mechanical and Automation Engineering, The Chinese University of Hong Kong, Hong Kong.

J. Zhou and Y.-H. Liu are also with the Hong Kong Center for Logistics Robotics, Hong Kong.

Q. Dou is with the Department of Computer Science and Engineering, The Chinese University of Hong Kong, Hong Kong.

rod theory [11], [29]. Gravagne *et al.* [27] and Frazelle *et al.* [30] explored the feedback linearization methods for dynamics control of continuum robots. The combinations of feedforward and feedback control have been proposed to maintain good accuracy and compliance for continuum robots [31]–[33]. Simaan *et al.* [34] and Bajo *et al.* [4] investigated inverse kinematics (IK) control schemes for telemanipulation of continuum robots in MIS. Camarillo *et al.* [28], Best *et al.* [35], and Khadem *et al.* [36] developed optimization-based control and model predictive control (MPC) approaches for continuum and soft robots, respectively, to avoid undesired configurations. In model-based methods, the modeling of continuum robots should be identified before implementation which would result in unknown deviations in the presence of backlash, friction, hysteresis, and tendon coupling. In addition, the strong assumptions of these models might not be validated with unexpected environmental disturbances. Nevertheless, Rucker and Webster III [29] derived statics and dynamics models coupling Cosserat rod and string models to account for external loads. Adaptive energy-shaping control of soft continuum robots [37] has emerged as a promising trend to compensate for disturbances with a port-Hamiltonian approach for modeling [38], while solving partial differential equations is regarded as one of the main challenges.

Model-free control strategies do not require a priori knowledge about the model of continuum robot and its modeling uncertainties, which are instead acquired by estimation methods. They are applicable to the highly nonlinear or nonuniform systems that can be affected by unknown environmental perturbations, making priori models invalid [7]. Rucker *et al.* [39] performed trajectory following of a steerable needle in the tissue using sliding mode control without a priori knowledge of model parameters. Yip and Camarillo [40], [41] proposed optimal control methods with optimization-based online estimations of the kinematics Jacobian and stiffness matrix of a continuum robot. An adaptive Kalman filter (KF) was adopted for a soft robot to update its Jacobian matrix, whose entries were assumed to vary linearly [42]. Alambeigi *et al.* [19], [24] presented a model-independent KF to estimate the deformation behavior of an unmodelled continuum robot by fusing eye-to-hand camera vision and FBG signals; lately, they introduced an optimization-based visual servoing of the robot with online model update using Broyden’s method.

With the advancements of artificial intelligence, control strategies employing machine learning, which can identify and learn the model/motion-based policies of continuum robots, have also gained great attention [43], [44]. Amongst, neural networks (NNs) are commonly utilized to solve IK models of continuum robots [9], [45]–[49]. Locally weighted projection regression (LWPR) and Gaussian process regression (GPR) have been also investigated as alternative approaches to approximate IK of soft continuum robot [50] for eye-in-hand visual servoing [51]. Thuruthel *et al.* [52] implemented reinforcement learning (RL) for soft robot control in which a dynamic model represented by a recurrent NN and sampled trajectory were adopted to learn control actions. Model-free RL algorithms are also developed to control soft robot by using simulation data instead of analytical modeling [53]–

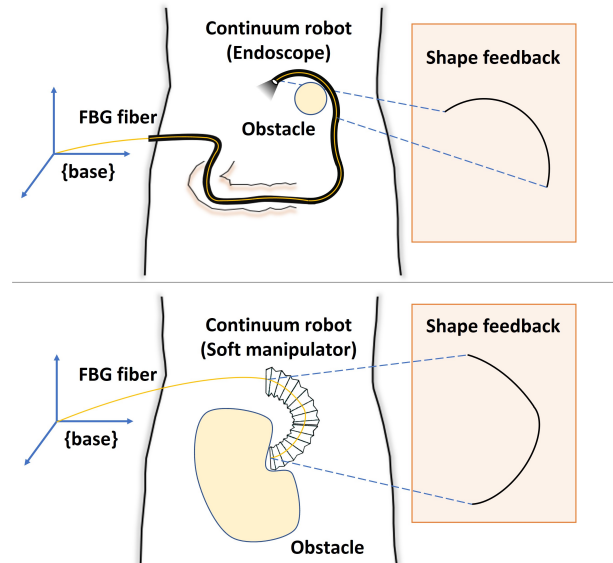


Fig. 1: Conceptual representation of 3-D shape sensing and control of continuum robots, e.g., endoscope (up), and soft manipulator (bottom), in unstructured environments.

[56]. Although these approaches alleviate the need for accurate modeling of continuum robots, large amounts of training data and offline identification are heavily required, hampering their practical deployments [44]. Due to probabilistic properties of these learning-based approaches, another major concern is the difficulty of deriving their stability conditions and even asymptotic convergences of control error and NN parameters [57], which may raise safety problems in unstructured contexts.

To guarantee convergent performance when using learning-based methods, Braganza *et al.* [31] utilized a NN to feedforward account for the nonlinear dynamics uncertainty in a soft continuum robot, while maintaining the boundedness of NN output together with the asymptotic convergence of tracking error under a nonlinear feedback controller. Tang *et al.* [57] developed an integration of iterative learning and MPC for soft robots that can online update the model parameters and guarantee the asymptotic stability of reference tracking, but they individually proved the convergences of estimated model parameters and tracking error, meaning that the convergence of tracking error cannot be guaranteed until the parameters were estimated to their true values. These hybrid controllers combine model-based and learning-based methods [58], in which most learning sectors aim to compensate for system uncertainties [59]. However, control strategies with stability analysis concerning the effect of modeling error caused by simultaneous model learning (during the convergence of estimated parameters) of continuum robots have not been reported [60], [61]. Nevertheless, Melingui *et al.* [62] addressed the stability of an adaptive NN controller that learns the kinematics of continuum robots, training an emulator is necessarily required before the control task. One more limitation of the existing solutions is that rigorous analysis in the presence of NN approximation error has not been considered [63], [64]. Moreover, although some existing methodologies have generic formulations for continuum robots, they were only validated

with motions in 2-D space by adding in-plane perturbations, while neglecting those out-of-plane ones, and thus without investigations in 3-D shape. 3-D shape servoing is to control the globally described shape of continuum robot to approach the target configuration, where the shape description can capture more characteristics of the robot than solely endpoint positions, providing better control accuracy for real applications, e.g., surgical tasks [24], [65]–[68]. Overall, there are open problems in 3-D shape control of continuum robots enabling them to perform complex tasks in sensitive environments [7], especially for robust and adaptive learning-based strategies, which are expected to integrate the advantages emphasized on: no priori data requirement, stability with convergences of both control error and model learning parameters, online error compensation, and accurate shape feedback [1], [44].

B. Contribution of this Paper

Towards these limitations, this paper proposes a robust data-driven control framework, which can automatically regulate the 3-D shape of the FBG-equipped continuum robot with unknown model in unstructured environments. To the best of the authors' knowledge, this is the first work in control of unmodeled continuum robots and soft continuum robots using 3-D shape feedback (e.g., FBG sensing), based on the development of a novel adaptive NN control strategy for online learning the robot's differential kinematics and simultaneous shape servoing. The proposed algorithm does not require priori data exploration and can concurrently guarantee the stability, convergent performance of control error and learning parameters, and online error compensation with unknown external conditions as compared with state-of-the-art methods [44]. The main contributions are summarized as follows:

- 1) A novel robust adaptive controller using FBG shape feedback is developed by taking advantage of nonlinear NNs approximation and a new NN-based shape flow predictor, to simultaneously learn the unknown differential kinematics of the robot, and to servo-control its 3-D shape against unexpected perturbations.
- 2) A novel composite adaptation algorithm is designed by jointly introducing the shape estimation error and shape flow error of the robot, to online update the NN weights and guarantee the NNs learning of the unknown model, and it can also account for the modeling error led by the estimated parameters during the convergence.
- 3) By taking the modeling error and NN approximation error into consideration, the stability of the closed-loop system with the asymptotic convergences of the shape control and estimation errors to zeros are rigorously proved using Lyapunov method, thus showing the convergence of the estimated NN parameters.
- 4) A robust and accurate filtering algorithm is hereby enhanced for 3-D shape sensing of the continuum robot by solely embedding a multi-core FBG fiber, which is self-contained, independent of external sensors (e.g., cameras), and maintains high sensing quality against disturbances. Additionally, more 3-D features computed from distributed FBG signals can be acquired for online model learning than only endpoint positions.

- 5) The proposed method has been comprehensively validated using two FBG-equipped continuum robots, including a robotic-assisted colonoscope system and multi-section extensible soft manipulators. The results demonstrate the versatility and adaptability of our algorithm in various unstructured environments and two phantom experiments for colonoscopy and oropharyngeal sampling.

The rest of this paper is organized as follows. Section II introduces the mathematical model. Section III details the proposed control algorithm. In Section IV and V, we present the experimental setup and results, respectively. Conclusion and future work are discussed in Section VI.

II. MATHEMATICAL MODELING

A. Problem Statement

In this work, we can trace 3-D positions of the points on the continuum robot using an FBG shape sensing system. The shape feature is extracted from the selected points' positions and utilized as the feedback signal for simultaneous model learning and shape servoing. Given a desired shape of the continuum robot, the objective is to design a velocity controller on the actuation input such that its shape asymptotically approaches to the desired one without any priori knowledge of the robot's model. We make the following remarks and assumption to further clarify the addressed problem.

Remark 1. *With the compact integration of FBG fiber into the entire continuum robot and robust shape sensing algorithm in this work, any point along its longitudinal direction can be traced to generate shape features.*

Remark 2. *The terminology "kinematics" in this paper can refer to the relationship between any point/shape feature on the continuum robot and its actuation input.*

Assumption 1. *The deformation behavior of the continuum robot is unknown, which specifically means that we have no priori and explicit identification of its model.*

B. Kinematics of Continuum Robots

To represent the state of the continuum robot in its configuration space, we first denote l points selected on the robot with their 3-D Cartesian positions $\mathbf{r}_i = [x_i \ y_i \ z_i]^T \in \mathbb{R}^3, i \in \{1, 2, \dots, l\}$, which are measured from the FBG sensors, and the actuator position input of the robot $\mathbf{q} = [q_1 \ q_1 \ \dots \ q_n]^T \in \mathbb{R}^n$. Then, we define a vector of the Cartesian positions of l selected points $\mathbf{r} \in \mathbb{R}^{3l}$ as

$$\mathbf{r} = [\mathbf{r}_1^T \ \mathbf{r}_2^T \ \dots \ \mathbf{r}_l^T]^T \quad (1)$$

The kinematics of the continuum robot mapping the selected points on the robot \mathbf{r} to the actuation position \mathbf{q} can be expressed by a smooth nonlinear unknown function as $\mathbf{r} = \mathbf{r}(\mathbf{q}) : \mathbb{R}^n \mapsto \mathbb{R}^{3l}$, the differential formulation of which as the differential kinematic equation yields

$$\dot{\mathbf{r}} = \mathbf{J}_r(\mathbf{q})\dot{\mathbf{q}} \quad (2)$$

where $\mathbf{J}_r(\mathbf{q}) \in \mathbb{R}^{3l \times n}$ represents the unknown Jacobian matrix of the continuum robot.

Assumption 2. The actuator velocity input of the continuum robot $\dot{\mathbf{q}}$ can be exactly set from the proposed controller, and its velocity $\dot{\mathbf{q}}$ and acceleration $\ddot{\mathbf{q}}$ are bounded [69].

C. Shape Feature Jacobian Matrix

Using the selected points $\mathbf{r}_i, i \in \{1, 2, \dots, l\}$ to describe the overall 3-D shape of the continuum robot, we construct a vector of shape feature as $\mathbf{x} = [x_1 \ x_2 \ \dots \ x_m]^\top \in \mathbb{R}^m$ with a smooth function $\mathbf{x} = \mathbf{x}(\mathbf{r}) : \mathbb{R}^{3l} \mapsto \mathbb{R}^m$, which will be explicitly defined in Section IV. The selected points' velocity $\dot{\mathbf{r}}$ can be related to the shape feature flow $\dot{\mathbf{x}} \in \mathbb{R}^m$ as

$$\dot{\mathbf{x}} = \mathbf{J}_x(\mathbf{r})\dot{\mathbf{r}} \quad (3)$$

where $\mathbf{J}_x(\mathbf{q}) \in \mathbb{R}^{m \times 3l}$ is the shape feature Jacobian matrix. In a combination of (2) and (3), we can relate the actuation velocity $\dot{\mathbf{q}}$ to the shape flow $\dot{\mathbf{x}}$ and take an unknown disturbance term $\mathbf{d} \in \mathbb{R}^m$ in consideration representing the system uncertainties and external disturbances in unstructured environments as

$$\dot{\mathbf{x}} = \underbrace{\mathbf{J}_x(\mathbf{r})\mathbf{J}_r(\mathbf{q})}_{\mathbf{J}_c(\mathbf{q})}\dot{\mathbf{q}} + \mathbf{d} \quad (4)$$

where $\mathbf{J}_c(\mathbf{q}) = \mathbf{J}_x(\mathbf{r})\mathbf{J}_r(\mathbf{q}) \in \mathbb{R}^{m \times n}$ is denoted as the combined deformation Jacobian matrix of the robot mapping its actuator velocity $\dot{\mathbf{q}}$ to the shape feedback flow $\dot{\mathbf{x}}$.

Assumption 3. The disturbance \mathbf{d} and its time derivative $\dot{\mathbf{d}}$ are bounded, and $\mathbf{d} \rightarrow \mathbf{0}$ as $\dot{\mathbf{q}} \rightarrow \mathbf{0}$ [70].

III. DATA-DRIVEN CONTROL ALGORITHM

A robust data-driven control strategy using FBG shape feedback and adaptive NNs approximation is designed for 3-D shape servoing of the continuum robot.

A. NNs Approximation to Combined Jacobian

Considering that the combined Jacobian matrix $\mathbf{J}_c(\mathbf{q})$ has unknown and time-varying elements, $\mathbf{J}_c(\mathbf{q})$ is hard to be directly estimated using a conventional adaptive mechanism. We adopt m adaptive NNs $\mathbf{W}_i\theta_i(\mathbf{q}), i \in \{1, 2, \dots, m\}$, employing radial basis functions (RBFs) [63], [71] to approximate m rows of $\mathbf{J}_c(\mathbf{q})$, respectively, with the actuation \mathbf{q} as input given by

$$\mathbf{J}_c(\mathbf{q}) = [\mathbf{W}_1\theta_1(\mathbf{q}) \ \mathbf{W}_2\theta_2(\mathbf{q}) \ \dots \ \mathbf{W}_m\theta_m(\mathbf{q})]^\top + \mathbf{E}_J \quad (5)$$

where $\mathbf{W}_i \in \mathbb{R}^{n \times k}, i \in \{1, 2, \dots, m\}$, represents the ideal weight matrix of the i -th NN with k neurons, $\theta_i(\mathbf{q}) \in \mathbb{R}^k, i \in \{1, 2, \dots, m\}$, is the corresponding vector of the activation functions, and the j -th neuron, $\theta_{ij}(\mathbf{q}), j \in \{1, 2, \dots, k\}$, of which is defined by a RBF as

$$\theta_{ij}(\mathbf{q}) = e^{-\frac{\|\mathbf{q} - \mu_{ij}\|^2}{\sigma_{ij}^2}} \quad (6)$$

where $\mu_{ij} \in \mathbb{R}^n$ is a vector representing the center value of the j -th neuron, and σ_{ij} is the corresponding width value, the basis of which can be determined according to the rough mapping from joint space to configuration space of continuum robot and detailed in Section IV. In (5), $\mathbf{E}_J \in \mathbb{R}^{m \times n}$ denotes a matrix representing the functional error of the NNs approximation,

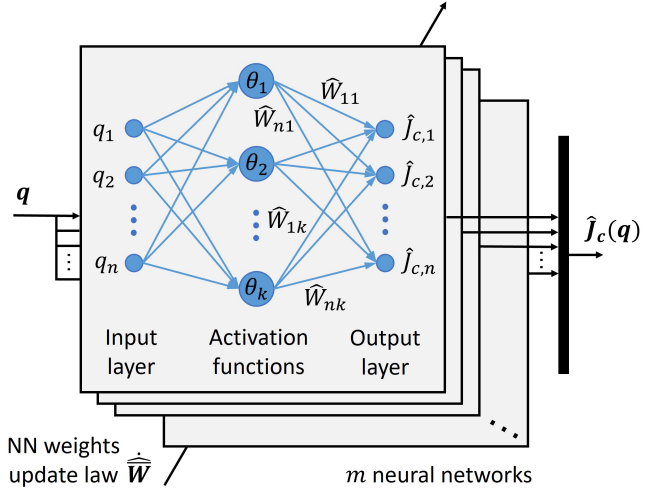


Fig. 2: m RBF NNs for Jacobian rows approximation, where for the i -th NN, $i \in \{1, 2, \dots, m\}$: $q_{j_q}, j_q \in \{1, 2, \dots, n\}$, represents the j_q -th element of \mathbf{q} , $\theta_{j_\theta}, j_\theta \in \{1, 2, \dots, k\}$, is the j_θ -th neuron of θ_i , $\hat{J}_{c,j_J}, j_J \in \{1, 2, \dots, n\}$, is the j_J -th element of the i -th row of $\hat{\mathbf{J}}_c$, and \hat{W}_{j_J, j_θ} is the (j_J, j_θ) -th element of $\hat{\mathbf{W}}_i$ updated by the adaptive law (25).

which is upper bounded and could decrease with the increase in the number of neurons k [63].

Using NNs approximation to the combined Jacobian matrix (5), the measurable shape flow $\dot{\mathbf{x}}$ using FBG sensing (4) can be further parameterized as

$$\dot{\mathbf{x}} = [\mathbf{W}_1\theta_1(\mathbf{q}) \ \mathbf{W}_2\theta_2(\mathbf{q}) \ \dots \ \mathbf{W}_m\theta_m(\mathbf{q})]^\top \dot{\mathbf{q}} + \boldsymbol{\delta} \quad (7)$$

where $\boldsymbol{\delta} \in \mathbb{R}^m$ is a combined perturbation term that describes the modeling disturbances \mathbf{d} together with NN approximation error \mathbf{E}_J given by

$$\boldsymbol{\delta} = \mathbf{E}_J\dot{\mathbf{q}} + \mathbf{d} \quad (8)$$

Considering **Assumption 2, 3**, and (8) with the boundedness of \mathbf{E}_J and its time derivative $\dot{\mathbf{E}}_J$ [63], we have the combined perturbation $\boldsymbol{\delta}$ and its time derivative $\dot{\boldsymbol{\delta}} \in \mathbb{R}^m$ are bounded as

$$\|\boldsymbol{\delta}\| \leq b_{\delta 1}, \quad \|\dot{\boldsymbol{\delta}}\| \leq b_{\delta 2} \quad (9)$$

where $b_{\delta 1}$ and $b_{\delta 2}$ are positive constants.

Since we do not have a priori knowledge of the deformation model of the continuum robot as well as the ideal NN weight matrices (i.e., $\mathbf{J}_c(\mathbf{q})$ and $\mathbf{W}_i, i \in \{1, 2, \dots, m\}$, are all unknown), we estimate the combined Jacobian matrix denoted by $\hat{\mathbf{J}}_c(\mathbf{q}) \in \mathbb{R}^{m \times n}$ using m estimated NNs $\hat{\mathbf{W}}_i\theta_i(\mathbf{q}), i \in \{1, 2, \dots, m\}$, as shown in Fig. 2 and expressed by

$$\hat{\mathbf{J}}_c(\mathbf{q}) = [\hat{\mathbf{W}}_1\theta_1(\mathbf{q}) \ \hat{\mathbf{W}}_2\theta_2(\mathbf{q}) \ \dots \ \hat{\mathbf{W}}_m\theta_m(\mathbf{q})]^\top \quad (10)$$

where $\hat{\mathbf{W}}_i \in \mathbb{R}^{n \times k}, i \in \{1, 2, \dots, m\}$, is the estimated NN weight matrix. To online tune the estimated NN weights and approximate the robot's model, a composite adaptation law for iterative evolution of the weights is proposed. The prediction error of the shape flow is minimized by a robust shape flow predictor, and two vectors of NN weights for linear parametrization of the ideal and estimated combined Jacobian matrices are defined, which are all derived in detail as follows.

B. Robust Shape Flow Predictor

To minimize the prediction error [61] of shape flow for learning the unknown differential kinematics of continuum robot in (4), we iteratively predict the shape flow denoted by $\hat{\mathbf{x}} \in \mathbb{R}^m$ and compare its difference with the measurable shape flow from FBG sensing results. For that, a robust shape flow predictor composed of the NNs approximation and the sliding mode method [61], [64] is derived as

$$\begin{aligned} \dot{\hat{\mathbf{x}}} &= \underbrace{\left[\widehat{\mathbf{W}}_1 \boldsymbol{\theta}_1(\mathbf{q}) \quad \widehat{\mathbf{W}}_2 \boldsymbol{\theta}_2(\mathbf{q}) \quad \cdots \quad \widehat{\mathbf{W}}_m \boldsymbol{\theta}_m(\mathbf{q}) \right]^\top}_{\widehat{\mathbf{J}}_c(\mathbf{q})} \dot{\mathbf{q}} \\ &+ \alpha_x \tilde{\mathbf{x}} + \beta_x \text{sat}(\tilde{\mathbf{x}}) \end{aligned} \quad (11)$$

where α_x and β_x are positive constants; $\text{sat}(\cdot)$ is a continuous saturation function as the smoothed implementation of sliding mode method, which can robustly remedy the system disturbances \mathbf{d} and NN approximation error \mathbf{E}_J , while avoiding chattering phenomenon [61]; and $\tilde{\mathbf{x}} \in \mathbb{R}^m$ represents the shape estimation error defined by

$$\tilde{\mathbf{x}} = \mathbf{x} - \hat{\mathbf{x}} \quad (12)$$

whose asymptotic convergence to zero can be guaranteed in the stability analysis. Taking the time derivative of $\tilde{\mathbf{x}}$ from (12), the prediction error [61] of shape flow defined as shape flow error $\tilde{\mathbf{x}} \in \mathbb{R}^m$, is derived from (11) and (12) as

$$\begin{aligned} \dot{\tilde{\mathbf{x}}} &= \dot{\mathbf{x}} - \dot{\hat{\mathbf{x}}} \\ &= \dot{\mathbf{x}} - \widehat{\mathbf{J}}_c(\mathbf{q}) \dot{\mathbf{q}} - \alpha_x \tilde{\mathbf{x}} - \beta_x \text{sat}(\tilde{\mathbf{x}}) \end{aligned} \quad (13)$$

which is acquired by calculating the difference between the FBG measurement $\dot{\mathbf{x}}$ and the predictor $\dot{\hat{\mathbf{x}}}$ using NN-estimated Jacobian $\widehat{\mathbf{J}}_c(\mathbf{q})$, actuation velocity $\dot{\mathbf{q}}$, together with the integral of the difference w.r.t. time, i.e., the shape estimation error $\tilde{\mathbf{x}}$, whose initial value is set by $\tilde{\mathbf{x}} = \mathbf{x}$ at $t = 0$ because we do not have a priori knowledge of it.

C. Vectors of NN Weight Matrices

We linearly parameterize the deformation model [69] in term of the NN weights to online update the unknown weights and learn the combined Jacobian for the controller. Let us group the columns of m ideal NN weight matrices \mathbf{W}_i and m estimated ones $\widehat{\mathbf{W}}_i$, $i \in \{1, 2, \dots, m\}$, respectively, into two vectors of them as $\overline{\mathbf{W}} \in \mathbb{R}^{kmn}$ and $\widehat{\overline{\mathbf{W}}} \in \mathbb{R}^{kmn}$ given by

$$\overline{\mathbf{W}} = [\mathbf{W}_{11}^\top \quad \mathbf{W}_{12}^\top \quad \cdots \quad \mathbf{W}_{1k}^\top \quad \mathbf{W}_{21}^\top \quad \cdots \quad \mathbf{W}_{mk}^\top]^\top \quad (14)$$

$$\widehat{\overline{\mathbf{W}}} = [\widehat{\mathbf{W}}_{11}^\top \quad \widehat{\mathbf{W}}_{12}^\top \quad \cdots \quad \widehat{\mathbf{W}}_{1k}^\top \quad \widehat{\mathbf{W}}_{21}^\top \quad \cdots \quad \widehat{\mathbf{W}}_{mk}^\top]^\top \quad (15)$$

where \mathbf{W}_{ij} and $\widehat{\mathbf{W}}_{ij}$ are the j -th columns, $j \in \{1, 2, \dots, k\}$, of the i -th ideal and estimated NN weight matrix \mathbf{W}_i and $\widehat{\mathbf{W}}_i$, $i \in \{1, 2, \dots, m\}$, respectively.

D. Composite Adaptation for Online NN Weights Estimation

Define two diagonal block matrices $\boldsymbol{\Theta}(\mathbf{q}) \in \mathbb{R}^{km \times m}$ and $\mathbf{Q}(\dot{\mathbf{q}}) \in \mathbb{R}^{kmn \times km}$, respectively, by grouping the activation functions $\boldsymbol{\theta}_i(\mathbf{q})$, $i \in \{1, 2, \dots, m\}$, and km actuator input $\dot{\mathbf{q}}$ as

$$\boldsymbol{\Theta}(\mathbf{q}) = \text{diag}(\underbrace{\boldsymbol{\theta}_1(\mathbf{q}), \boldsymbol{\theta}_2(\mathbf{q}), \cdots, \boldsymbol{\theta}_m(\mathbf{q})}_{\boldsymbol{\theta}_i(\mathbf{q}), i \in \{1, 2, \dots, m\}}) \quad (16)$$

$$\mathbf{Q}(\dot{\mathbf{q}}) = \text{diag}(\underbrace{\dot{\mathbf{q}}, \dot{\mathbf{q}}, \cdots, \dot{\mathbf{q}}}_{km \dot{\mathbf{q}}}) \quad (17)$$

The first term of the FBG-measured shape flow $\dot{\mathbf{x}}$ in (7) approximated by the ideal NNs can be linearly parameterized using (14), (16), and (17), given by

$$\begin{aligned} &[\mathbf{W}_1 \boldsymbol{\theta}_1(\mathbf{q}) \quad \mathbf{W}_2 \boldsymbol{\theta}_2(\mathbf{q}) \quad \cdots \quad \mathbf{W}_m \boldsymbol{\theta}_m(\mathbf{q})]^\top \dot{\mathbf{q}} \\ &= \boldsymbol{\Theta}^\top(\mathbf{q}) [\mathbf{W}_1 \quad \mathbf{W}_2 \quad \cdots \quad \mathbf{W}_m]^\top \dot{\mathbf{q}} \\ &= \boldsymbol{\Theta}^\top(\mathbf{q}) \mathbf{Q}^\top(\dot{\mathbf{q}}) \overline{\mathbf{W}} \end{aligned} \quad (18)$$

as well as the NNs approximation of the predicted shape flow $\dot{\hat{\mathbf{x}}}$ in (11) formulated as

$$[\widehat{\mathbf{W}}_1 \boldsymbol{\theta}_1(\mathbf{q}) \quad \widehat{\mathbf{W}}_2 \boldsymbol{\theta}_2(\mathbf{q}) \quad \cdots \quad \widehat{\mathbf{W}}_m \boldsymbol{\theta}_m(\mathbf{q})]^\top \dot{\mathbf{q}} = \boldsymbol{\Theta}^\top(\mathbf{q}) \mathbf{Q}^\top(\dot{\mathbf{q}}) \widehat{\overline{\mathbf{W}}} \quad (19)$$

where $\boldsymbol{\Theta}^\top(\mathbf{q}) \mathbf{Q}^\top(\dot{\mathbf{q}})$ is also equivalent to $\boldsymbol{\Theta}^\top(\mathbf{q}) \otimes \dot{\mathbf{q}}^\top$ using Kronecker Product [19]. Then the measurable shape flow $\dot{\mathbf{x}}$ in (7) and the predicted one $\dot{\hat{\mathbf{x}}}$ in (11) can be expressed, respectively, using the linearly parameterized formulation (18) and (19) as

$$\dot{\mathbf{x}} = \boldsymbol{\Theta}^\top(\mathbf{q}) \mathbf{Q}^\top(\dot{\mathbf{q}}) \overline{\mathbf{W}} + \boldsymbol{\delta} \quad (20)$$

$$\dot{\hat{\mathbf{x}}} = \boldsymbol{\Theta}^\top(\mathbf{q}) \mathbf{Q}^\top(\dot{\mathbf{q}}) \widehat{\overline{\mathbf{W}}} + \alpha_x \tilde{\mathbf{x}} + \beta_x \text{sat}(\tilde{\mathbf{x}}) \quad (21)$$

and the difference between the ideal and estimated NNs approximations to the combined Jacobian matrices multiplying the actuation velocity $\dot{\mathbf{q}}$, i.e., the difference between $\mathbf{J}_c(\mathbf{q}) \dot{\mathbf{q}}$ and $\widehat{\mathbf{J}}_c(\mathbf{q}) \dot{\mathbf{q}}$, is calculated by

$$\mathbf{J}_c(\mathbf{q}) \dot{\mathbf{q}} - \widehat{\mathbf{J}}_c(\mathbf{q}) \dot{\mathbf{q}} = \boldsymbol{\Theta}^\top(\mathbf{q}) \mathbf{Q}^\top(\dot{\mathbf{q}}) \widetilde{\overline{\mathbf{W}}} + \mathbf{E}_J \dot{\mathbf{q}} \quad (22)$$

where $\widetilde{\overline{\mathbf{W}}} = \overline{\mathbf{W}} - \widehat{\overline{\mathbf{W}}} \in \mathbb{R}^{kmn}$ denotes the estimation error of NN weights in vector form. From (20) and (21), we can further derive the linearly parameterized shape flow error $\tilde{\mathbf{x}}$ in (13) as

$$\dot{\tilde{\mathbf{x}}} = \boldsymbol{\Theta}^\top(\mathbf{q}) \mathbf{Q}^\top(\dot{\mathbf{q}}) \widetilde{\overline{\mathbf{W}}} + \boldsymbol{\delta} - \alpha_x \tilde{\mathbf{x}} - \beta_x \text{sat}(\tilde{\mathbf{x}}) \quad (23)$$

In addition to the above derivations for the adaptive update of the NN weights, we introduce the filtered shape estimation error $\mathbf{r}_x \in \mathbb{R}^m$ from (23) defined by

$$\mathbf{r}_x = \dot{\tilde{\mathbf{x}}} + \alpha_x \tilde{\mathbf{x}} = \boldsymbol{\Theta}^\top(\mathbf{q}) \mathbf{Q}^\top(\dot{\mathbf{q}}) \widetilde{\overline{\mathbf{W}}} + \boldsymbol{\delta} - \beta_x \text{sat}(\tilde{\mathbf{x}}) \quad (24)$$

which can be minimized using the following adaptation law and is available to ensure the asymptotic regulation of the shape flow error $\tilde{\mathbf{x}}$ compared with other forms difficult for this objective, e.g., simply $\dot{\tilde{\mathbf{x}}}$.

Consequently, the vector of the estimated NN weights $\widehat{\overline{\mathbf{W}}}$ can be iteratively updated by using a composite adaptation rule modified from Slotine–Li method in [61] and proposed as

$$\begin{aligned} \dot{\widehat{\overline{\mathbf{W}}}} &= \Gamma_W^{-1} \text{proj} \left\{ k_e \mathbf{Q}(\dot{\mathbf{q}}) \boldsymbol{\Theta}(\mathbf{q}) \mathbf{e} \right. \\ &\quad \left. + k_x \mathbf{Q}(\dot{\mathbf{q}}) \boldsymbol{\Theta}(\mathbf{q}) \tilde{\mathbf{x}} + k_r \mathbf{Q}(\dot{\mathbf{q}}) \boldsymbol{\Theta}(\mathbf{q}) \mathbf{r}_x \right\} \end{aligned} \quad (25)$$

where k_e , k_x , and k_r are positive constants, Γ_W is a positive definite and diagonal gain matrix, $\mathbf{e} = \mathbf{x} - \mathbf{x}_d \in \mathbb{R}^m$ denotes the FBG-shape feedback error (control error), $\mathbf{x}_d \in \mathbb{R}^m$ represents the desired shape of the continuum robot, and $\text{proj}\{\cdot\}$ is a projection operator to guarantee the estimated NN weights

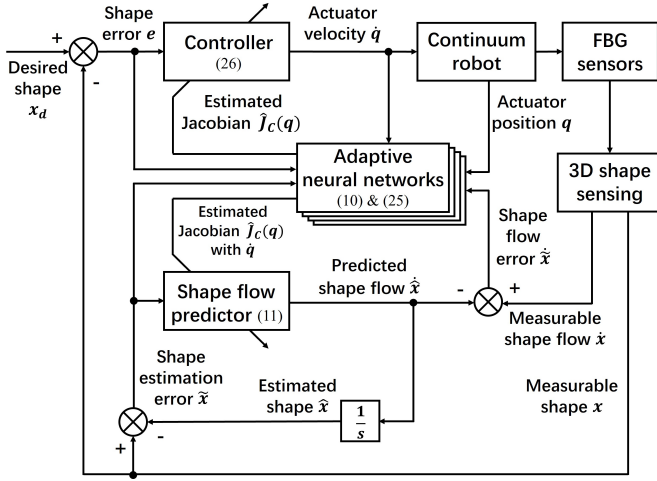


Fig. 3: Block diagram of the closed-loop system under the proposed control algorithm.

bounded [72]. In (25), the first term of the shape control error is for the compensation of the difference between the estimated and real Jacobian matrices. The second term of the shape estimation error is to account for a cross term in the stability analysis. The third term about the filtered shape estimation error is for the online gradient descending minimization of the errors about the estimated model parameters.

E. Controller Design and Stability Analysis

Constructing the estimated combined Jacobian $\hat{J}_c(q)$ from the updated NNs by (10), the controller is derived as

$$\dot{q} = -k_c \hat{J}_c^+(q) e - k_s \hat{J}_c^+(q) \text{sat}(e) \quad (26)$$

where k_c and k_s are positive constants, $\hat{J}_c^+(q) \in \mathbb{R}^{n \times m}$ represents the Moore–Penrose pseudo-inverse of $\hat{J}_c(q)$, and e is the shape control error. In (26), the second term using a continuous saturation function is designed to eliminate the combined perturbations δ in the measurement flow. The implementation of the proposed shape servoing algorithm is detailed in Appendix A, and the block diagram of the close-loop system under the proposed adaptive controller with NNs approximation is demonstrated in Fig. 3.

Theorem 1. *Under the proposed shape flow predictor (11), composite adaptive algorithm (25), and velocity controller (26), the closed-loop system gives rise to all the convergences of the shape control error e , shape estimation error \tilde{x} , and shape flow error $\tilde{\dot{x}}$ to zeros as $t \rightarrow \infty$, i.e.,*

$$\lim_{t \rightarrow \infty} e = 0, \quad \lim_{t \rightarrow \infty} \tilde{x} = 0, \quad \lim_{t \rightarrow \infty} \tilde{\dot{x}} = 0 \quad (27)$$

together with the convergence of estimated NN weights \hat{W}_i , $i \in \{1, 2, \dots, m\}$, and guaranteed NNs learning of the unknown model, if the predictor parameters α_x , β_x , and controller parameter k_s are chosen such that

$$k_s \geq b_{\delta 1}, \quad \beta_x \geq b_{\delta 1} + \frac{b_{\delta 2}}{\alpha_x} \quad (28)$$

where $b_{\delta 1}$ and $b_{\delta 2}$ are positive constants introduced in (9).

Proof. Define a Lyapunov candidate function as

$$\mathcal{V} = \frac{1}{2} k_e e^T e + \frac{1}{2} k_x \tilde{x}^T \tilde{x} + \frac{1}{2} \tilde{W}^T \Gamma_W \tilde{W} + k_r \mathcal{R} \quad (29)$$

with the auxiliary function $\mathcal{R}(t)$ defined as

$$\mathcal{R}(t) = \beta_x \sum_{i=1}^m |\tilde{x}_i(0)| - \tilde{x}^T(0) \delta(0) - \mathcal{H}(t) + \mathcal{H}(0) \quad (30)$$

where $i = 1, 2, \dots, m$ represents the i -th element of \tilde{x} , and the auxiliary function $\mathcal{H}(t)$ [64] is generated by

$$\dot{\mathcal{H}} = \mathbf{r}_x^T (\delta - \beta_x \text{sat}(\tilde{x})) \quad (31)$$

The time derivative of $\mathcal{R}(t)$ is derived as

$$\dot{\mathcal{R}} = -\dot{\mathcal{H}} = -\mathbf{r}_x^T (\delta - \beta_x \text{sat}(\tilde{x})) \quad (32)$$

and $\mathcal{R}(t)$ is positive semi-definite if the sufficient condition

$$\beta_x \geq b_{\delta 1} + \frac{b_{\delta 2}}{\alpha_x} \quad (33)$$

in (28) is satisfied, which is proved in Appendix B.

Differentiating \mathcal{V} in (29) and substituting (4), (23), (25), and (32) results in

$$\begin{aligned} \dot{\mathcal{V}} &= k_e e^T (J_c(q) \dot{q} + d) + k_x \tilde{x}^T \Theta^T(q) Q^T(\dot{q}) \tilde{W} \\ &\quad + k_x \tilde{x}^T (\delta - \alpha_x \tilde{x} - \beta_x \text{sat}(\tilde{x})) - \tilde{W}^T \left(k_x Q(\dot{q}) \Theta(q) \tilde{x} \right. \\ &\quad \left. + k_e Q(\dot{q}) \Theta(q) e + k_r Q(\dot{q}) \Theta(q) r_x \right) \\ &\quad - k_r \mathbf{r}_x^T (\delta - \beta_x \text{sat}(\tilde{x})) \\ &= -k_x \alpha_x \tilde{x}^T \tilde{x} + k_x \tilde{x}^T (\delta - \beta_x \text{sat}(\tilde{x})) + k_e e^T J_c(q) \dot{q} \\ &\quad + k_e e^T d - k_e \tilde{W}^T Q(\dot{q}) \Theta(q) e - k_r \tilde{W}^T Q(\dot{q}) \Theta(q) r_x \\ &\quad - k_r \mathbf{r}_x^T (\delta - \beta_x \text{sat}(\tilde{x})) \end{aligned} \quad (34)$$

Substituting (22) and (24) into (34), we have

$$\begin{aligned} \dot{\mathcal{V}} &= -k_x \alpha_x \tilde{x}^T \tilde{x} + k_x \tilde{x}^T (\delta - \beta_x \text{sat}(\tilde{x})) + k_e e^T J_c(q) \dot{q} \\ &\quad + k_e e^T d - k_e e^T \left(J_c(q) \dot{q} - \hat{J}_c(q) \dot{q} - E_J \dot{q} \right) \\ &\quad - k_r \mathbf{r}_x^T (r_x - \delta + \beta_x \text{sat}(\tilde{x})) - k_r \mathbf{r}_x^T (\delta - \beta_x \text{sat}(\tilde{x})) \\ &= -k_x \alpha_x \tilde{x}^T \tilde{x} + k_x \tilde{x}^T (\delta - \beta_x \text{sat}(\tilde{x})) + k_e e^T \hat{J}_c(q) \dot{q} \\ &\quad + k_e e^T \delta - k_r \mathbf{r}_x^T r_x \end{aligned} \quad (35)$$

Using the controller (26) and taking the upper bound with (9), we can further have

$$\begin{aligned} \dot{\mathcal{V}} &= -k_x \alpha_x \tilde{x}^T \tilde{x} + k_x \tilde{x}^T (\delta - \beta_x \text{sat}(\tilde{x})) \\ &\quad + k_e e^T \delta - k_e e^T (k_c e + k_s \text{sat}(e)) - k_r \mathbf{r}_x^T r_x \\ &\leq -k_x \alpha_x \tilde{x}^T \tilde{x} - k_x (\beta_x - b_{\delta 1}) \|\tilde{x}\| - k_e k_c e^T e \\ &\quad - k_e (k_s - b_{\delta 1}) \|e\| - k_r \mathbf{r}_x^T r_x \end{aligned} \quad (36)$$

From (33), we can conclude that $-k_x (\beta_x - b_{\delta 1}) \|\tilde{x}\| \leq 0$ since the condition is satisfied as

$$\beta_x \geq b_{\delta 1} + \frac{b_{\delta 2}}{\alpha_x} \geq b_{\delta 1} \quad (37)$$

If the controller parameter k_s is chosen sufficiently large such that $k_s \geq b_{\delta 1}$ in (28) is satisfied, we have

$-k_e(k_s - b_{\delta 1})\|e\| \leq 0$ and obtain that

$$\dot{\mathcal{V}} \leq -k_x \alpha_x \tilde{x}^\top \tilde{x} - k_c k_c e^\top e - k_r r_x^\top r_x \leq 0 \quad (38)$$

Since $\mathcal{V} > 0$ and $\dot{\mathcal{V}} \leq 0$, \mathcal{V} is bounded, which directly implies that the shape control error e , shape estimation error \tilde{x} , and estimation error of NN weights \tilde{W} are all bounded. The boundedness of \dot{q} by **Assumption 2**, and the boundedness of activation functions $\theta_i(q)$, $i \in \{1, 2, \dots, m\}$ as well as their derivatives w.r.t. the corresponding arguments [63] guarantee the boundedness of Θ and $\dot{\Theta}$ from (16). Because Q and δ are bounded by (17) and (9), respectively, their boundedness together with those of Θ , \tilde{W} , \tilde{x} , and $\text{sat}(\cdot)$ function ensure that the shape flow error \tilde{x} is bounded from (23). From (24), the boundedness of \tilde{x} and \tilde{x} implies the boundedness of the filtered shape estimation error r_x . The $\text{proj}(\cdot)$ function in (25) indicates the boundedness of \tilde{W} , \tilde{W} , and \tilde{W} . Since \dot{q} and \ddot{q} are bounded, and so are W_i , $\theta_i(q)$, $i \in \{1, 2, \dots, m\}$, and E_J [63], $J_c(q)$ and \dot{Q} are bounded from (5) and (17), respectively. From (4), the boundedness of \dot{q} , $J_c(q)$, and d also indicates that the shape feature is varied continuously, i.e., \dot{x} is bounded and so is \dot{e} . Since Θ , $\dot{\Theta}$, Q , \dot{Q} , \tilde{W} , \tilde{W} , δ from (9), $\text{sat}(\cdot)$ function with its derivative w.r.t. \tilde{x} , and \tilde{x} are all bounded, we can conclude that \dot{r}_x is bounded from the time derivative of (24). Therefore, e , \tilde{x} , and r_x are uniformly continuous. By Barbalat's lemma, we can prove that

$$\lim_{t \rightarrow \infty} e = 0, \quad \lim_{t \rightarrow \infty} r_x = 0, \quad \lim_{t \rightarrow \infty} \tilde{x} = 0 \quad (39)$$

As $t \rightarrow \infty$, since $r_x \rightarrow 0$ and $\tilde{x} \rightarrow 0$, we have $\dot{\tilde{x}} \rightarrow 0$ following (24). From (23), we can prove the asymptotic minimization of the estimation error of NN weights \tilde{W} [73]. Consequently, the shape control error, shape estimation error, and shape flow error are all convergent to zeros, and the online learning of the combined Jacobian $J_c(q)$ using our adaptive NNs approximation is guaranteed. ■

IV. EXPERIMENTAL SETUP

To evaluate the proposed control algorithm, a comprehensive experimental study has been performed. We introduce the setup in this section, including basic features for shape descriptions, two platforms, FBG sensing system, and initialization.

A. Basic Shape Features

Two basic shape features including point's position, and bending/twist angles are defined, which can be composed to globally describe the shape of continuum robot.

1) *Point's position*: Point's position refers directly to the Cartesian position $r_i = [x_i \ y_i \ z_i]^\top \in \mathbb{R}^3$, $i \in \{1, 2, \dots, l\}$, selected on the continuum robot, which can also be utilized to construct the bending and twist angles as follows.

2) *Bending/twist angles*: Bending/twist angles consist of bending angle κ and twist angle φ , which describe the deflection and torsion of one robot's section, respectively. Bending angle $\kappa \in \mathbb{R}$, for $0^\circ < \kappa \leq 180^\circ$, is a scalar that describes the angle between two intersecting lines constructed from three reference points r_i , $i \in \{1, 2, 3\}$, as shown in Fig. 4 (a). Similar to the folding angle in [69], the bending angle is

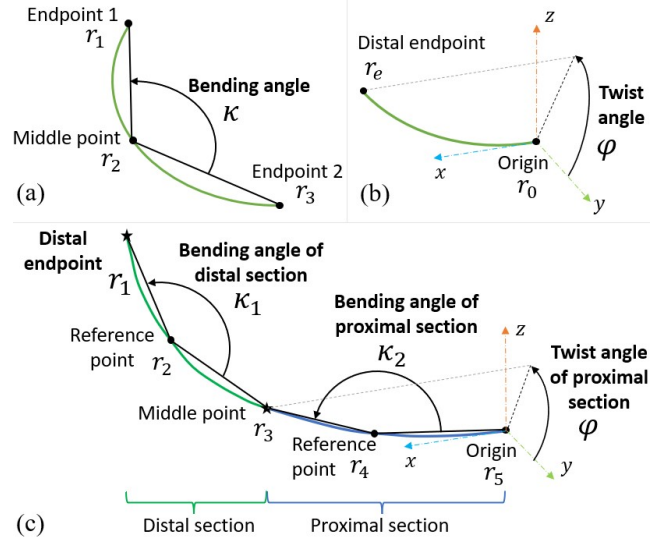


Fig. 4: Basic shape features: (a) bending angle and (b) twist angle. Shape feature for multi-section manipulator: (c) distal endpoint position with bending/twist angles (DEP-BTA).

$$\kappa = \arccos \left(\frac{(r_1 - r_2) \cdot (r_3 - r_2)}{\|r_1 - r_2\| \|r_3 - r_2\|} \right) \quad (40)$$

where r_1 and r_3 represent two endpoints of the section, and r_2 is a middle point chosen on the robot, which are determined in the initialization phase. It should be noted that different bending angles of the same robot's deformation can be described by selecting different middle point r_2 . Twist angle $\varphi \in \mathbb{R}$, for $-180^\circ < \varphi \leq 180^\circ$, describes the rotation about the x-axis of the base frame as shown in Fig. 4 (b). By using the section's endpoint $r_e = [x_e \ y_e \ z_e]^\top \in \mathbb{R}^3$, φ is

$$\varphi = \text{atan2}(z_e, y_e) \quad (41)$$

B. Robotic-Assisted Colonoscope System

We integrated a robotic-assisted colonoscope system previously reported in [22], of which the distal continuum mechanism with 120 mm working length and 12.9 mm outer diameter was employed to perform the experimental study, as shown in Fig. 5. An FBG fiber was embedded in the colonoscope channel. A dial drive module was designed to control the deflection motions of the continuum mechanism with 2 DOFs (i.e., $n = 2$). The zero actuator position forming the continuum mechanism a straight line with a bending angle of 180° (i.e., $\kappa = 180^\circ$) as the initial shape is $q_0 = [2400 \ 2000]^\top \in \mathbb{R}^2$.

To globally describe the deformation of the distal continuum mechanism, two shape features are defined including (a) two points' positions and (b) bending/twist angles. The feature of two points' positions $x \in \mathbb{R}^6$ is constructed by stacking the Cartesian position of the distal endpoint $r_{e1} \in \mathbb{R}^3$ and that of the middle point $r_{e2} \in \mathbb{R}^3$ given by

$$x = [r_{e1}^\top \ r_{e2}^\top]^\top \quad (42)$$

and the bending/twist angles $x \in \mathbb{R}^2$ consist of the bending angle κ and twist angle φ in (40) and (41), respectively, as

$$x = [\kappa \ \varphi]^\top \quad (43)$$

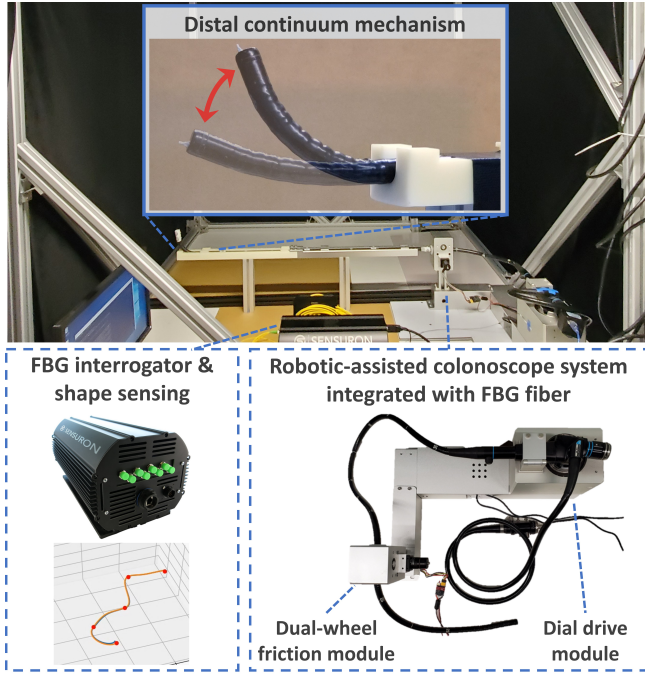


Fig. 5: Experimental platform: robotic-assisted colonoscope system integrated with multi-core FBG fiber.

C. Multi-Section Extensible Soft Manipulator

A soft continuum manipulator with two extensible sections and 6 DOFs in total (i.e., $n = 6$), has been integrated and deployed for the experimental study as shown in Fig. 6. The soft manipulator has an outer diameter of 60 mm, a working length of 180 mm, and a central channel to embed FBG fiber. Its extensible continuum section, including outer and inner backbones fabricated by 3-D printing with soft materials (CR-TPU 1.75 mm) and capable of omni-directional deflections under variable stiffness/length, was previously designed and employed as a wrist component of a tele-operated robotic platform for oropharyngeal swabs sampling [74]. The deflection motions of each soft section are driven by three cables and actuated by servo motors (Hiwonder LX-15D) with the zero position as $\mathbf{q}_0 = [240 \ 240 \ 240 \ 660 \ 660 \ 660]^T \in \mathbb{R}^6$. Filled with small particles in the inner chamber (backbone) of the soft section [75], its stiffness/length can be adjusted by pulling/pushing three cables together.

Besides two points' positions $\mathbf{x} \in \mathbb{R}^6$ as a type of shape feature denoted in (42), another shape feature called distal endpoint position with bending/twist angles (DEP-BTA) $\mathbf{x} \in \mathbb{R}^6$ is defined by stacking the Cartesian position of distal endpoint $\mathbf{r}_1 \in \mathbb{R}^3$ and three angles $\boldsymbol{\xi} \in \mathbb{R}^3$, including two bending angles of distal section κ_1 and proximal section κ_2 , and one twist angle of proximal section φ , as shown in Fig. 4 (c) by

$$\mathbf{x} = [\mathbf{r}_1^T \ \boldsymbol{\xi}^T]^T, \quad \boldsymbol{\xi} = [\kappa_1 \ \kappa_2 \ \varphi]^T \quad (44)$$

where \mathbf{r}_1 can locate the desired distal endpoint and determine the total length of soft robot, κ_1 and κ_2 are utilized to describe the deflections of both sections, and φ can determine the direction of the intersection point of two sections paralleled with the base plane (i.e., yz-plane in Fig. 4 (c)).

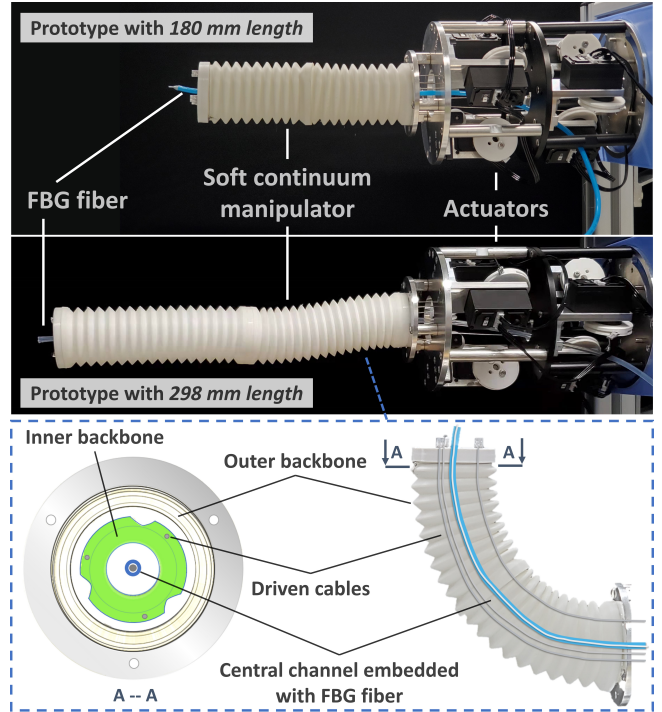


Fig. 6: Experimental platform: soft continuum manipulator equipped with multi-core FBG fiber.

D. FBG Shape Sensing System

To acquire the 3-D shape of the continuum robots, two 4-core all grating FBG fibers (FBGS International) with outer diameters of 190 μm were separately integrated into the inner channels of two robots. Note that such a small fiber diameter makes it feasible to be embedded into various types of flexible surgical instruments, e.g., steerable needles and catheters [15]. The fiber has 1 center core and 3 outer cores positioned at 120° with 37 μm distance to the center. We used an interrogator (RTS125+, Sensuron) to simultaneously decode strains from 45 and 55 FBG-sections of two robots, respectively, with both 30 Hz acquisition frequency and 3.3 mm spatial resolution.

Robust and accurate shape sensing results can be acquired by employing a modified version of previous algorithm [22] with 25 Hz sensing frequency. The frequency of the overall closed-loop system under the proposed controller is 20 Hz, which is regarded as comparable with those in [19], [24].

E. Initialization

The parameters adopted in the study using the colonoscope system were set as follows: the controller $k_c = 0.32$ and $k_s = 0.04$. For NNs approximation, we used 9 neurons for each NN (i.e., $k = 9$) and RBFs (6) as their activation functions, which are commonly used for adaptive NN control [63], [71]. We then chose a set of basis of center values $\boldsymbol{\mu}_{0j} \in \mathbb{R}^2$, $j \in \{1, 2, \dots, 9\}$, which are expressed in the robot's joint space and can be mapped to eight approximately equal quadrants of the Cartesian workspace of robot's distal endpoint, and a set of basis of width values σ_{0j} , $j \in \{1, 2, \dots, 9\}$, which represents the coverage scope of the neuron input with the corresponding center, i.e., approximated spacing between consecutive centers in the joint space. The details of these bases can be found in Appendix C. The center values $\boldsymbol{\mu}_{ij} \in \mathbb{R}^2$

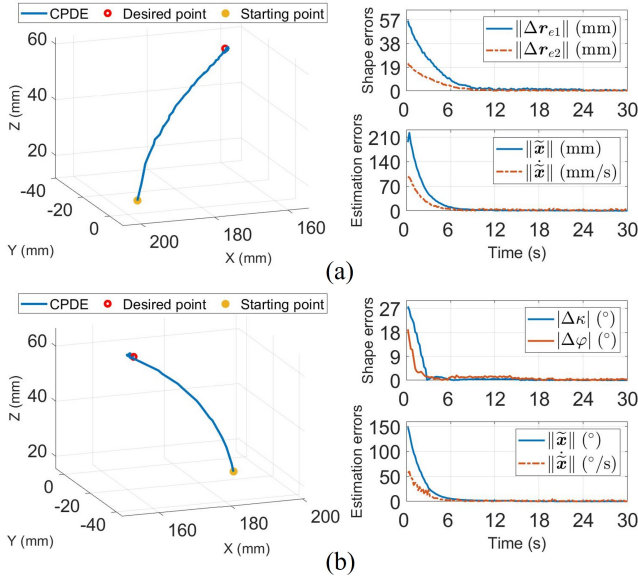


Fig. 7: CPDE (left) and shape errors (right) of experiments using colonoscope system in free environments, with (a) two points (42) and (b) bending/twist angles (43) as shape features.

of the i -th NN, $i \in \{1, 2\}$, in our experiments were initialized by randomly sorting the columns of the basis, and so were the corresponding widths σ_{ij} , which aims to prevent the rows of the combined Jacobian from being linearly dependent. This can consequently avoid the Jacobian ill-conditioned or even singular, eliminating overspeed motions during the tasks.

In the experiments using the soft manipulator, the parameters were accordingly set as: $\alpha_x = 0.6$ and $\beta_x = 0.12$; $k_e = 0.01$, $k_x = 0.01$, $k_r = 0.2$, and $\Gamma_W^{-1} = \mathbf{I}_{78m \times 78m} \in \mathbb{R}^{78m \times 78m}$ as an identity matrix; $k_c = 0.02$ and $k_s = 0.01$. These parameters were tuned based on the preliminary experimental results providing the desired performance with convergences of shape control and estimation errors to zeros, which is similar to the tuning method in [69]. When testing with this soft robot, 13 neurons were utilized for each NN (i.e., $k = 13$). A set of basis of centers $\mu_{0j} \in \mathbb{R}^6$, $j \in \{1, 2, \dots, 13\}$, which belong to around twelve quadrants of endpoint workspace, as well as the corresponding basis of widths σ_{0j} , were chosen and listed in Appendix C. In these experiments, the center values $\mu_{ij} \in \mathbb{R}^6$ together with the corresponding width values σ_{ij} , $i \in \{1, 2, \dots, 6\}$, were initialized in the same way as they were when using the colonoscope system.

Given that there was no requirement of a priori identification of the robot's model, we initialized the estimated shape by zeros, i.e., $\hat{\mathbf{x}} = \mathbf{0}_{m \times 1}$. To enable fast learning convergence and improve the transient performance of the proposed NN-based algorithm, a normalized initialization method [76] was utilized to initialize the NN weights, i.e., $\widehat{\mathbf{W}}_i$, $i \in \{1, 2, \dots, m\}$ at $t = 0$. Then, we conducted a few iterations of continuous slow motions in a small region around the initial configuration in the free environments [69], [70], which can speed up the convergence during 3-D shape servoing.

V. EXPERIMENTAL RESULTS

Experimental validations (29 experiments in total) were performed to evaluate the performance of the proposed algorithm,

including general tasks (20 experiments) using two continuum robots in free and unstructured environments, special validations (3 experiments), comparison tasks (4 experiments), and case studies in medical contexts (2 experiments). We constructed two shape features for each robot using the descriptions (42), (43), and (44). The results including Cartesian path of the robot's distal endpoint (CPDE), as well as 2-norms of shape errors, i.e., those of shape servoed errors $\|e\|$, shape estimation errors $\|\tilde{\mathbf{x}}\|$, and shape flow errors $\|\tilde{\dot{\mathbf{x}}}\|$, are recorded and presented. Considering that the distal endpoint has the largest range of motion among the points on the robot, its Cartesian path is chosen to be emphasized and demonstrated in all experiments rather than the convergence of overall shape. The ranks of the matrix $\tilde{\mathbf{J}}_c(\mathbf{q})\tilde{\mathbf{J}}_c^+(\mathbf{q}) \in \mathbb{R}^{m \times m}$ were monitored to prevent its reduction, which weakens the robot's manipulability. The control inputs $\dot{\mathbf{q}}$ from (26) were recorded to avoid too fast instantaneous velocity of the actuators. We attach a video emphasizing the exterior views of the continuum robots and their simultaneous FBG-shape convergences.

For all experimental figures showing CPDE and shape errors except special explanations, we make the following notes:

- 1) The left plots show CPDE by blue curves, and the corresponding desired and starting points by red and yellow points, respectively.
- 2) The top-right plots demonstrate the shape control errors using different shape descriptions. For those described by two points (42), the blue and red curves represent the 2-norms of Cartesian position errors $\Delta \mathbf{r}_{e1}, \Delta \mathbf{r}_{e2} \in \mathbb{R}^3$ of the endpoint \mathbf{r}_{e1} and middle point \mathbf{r}_{e2} , respectively.
- 3) In the top-right plots when using colonoscope system with bending/twist angles (43) as shape feature, the blue and red curves represent the absolute values of bending and twist error $\Delta \kappa, \Delta \varphi \in \mathbb{R}$ from (40) and (41), respectively. For those using soft manipulator described by DEP-BTA (44), the blue and red curves represent the 2-norms of position error of distal endpoint $\Delta \mathbf{r}_1 \in \mathbb{R}^3$ and bending/twist error $\Delta \xi \in \mathbb{R}^3$, respectively.
- 4) In the bottom-right plots showing estimated errors, the blue and red curves represent the 2-norms of shape estimation error $\tilde{\mathbf{x}}$ and shape flow error $\tilde{\dot{\mathbf{x}}}$, respectively.

A. Shape Servoing Tasks in Free Environments

We conducted the shape control tasks in free space using the colonoscope system and soft manipulator, respectively, and the resulting CPDE and shape errors are depicted in Fig. 7 and Fig. 8. Since two features were used to describe the shape of each robot, the results using two points (42) are presented in figures (a), and those using another feature (43)/(44) are demonstrated in figures (b). In the left plots of Fig. 7 demonstrating CPDE using the colonoscope system, distal endpoints can approach the desired position with two shape features, though we control the shape without distal endpoint positioning when described by bending/twist angles. The right images indicate the asymptotic minimization of shape servoed and estimated errors regardless of different shape descriptions, from which we can observe that the 3-D shape of continuum mechanism can automatically converge to the desired one.

Given that the length of soft manipulator can be adjusted as described above, the arc lengths of its initial and desired shapes

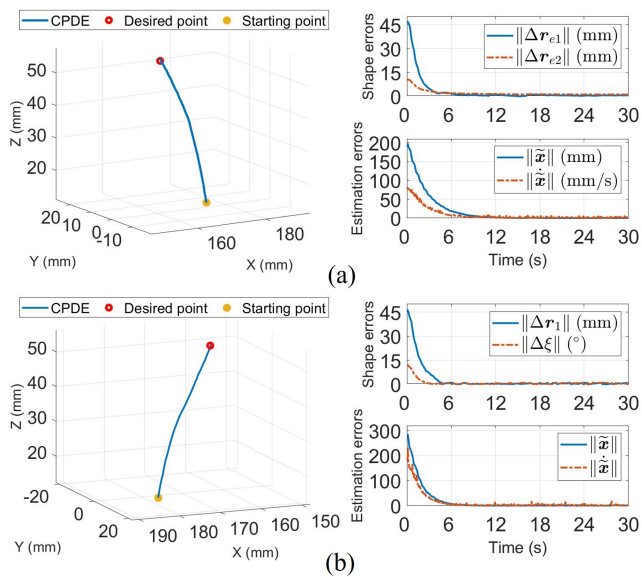


Fig. 8: CPDE (left) and shape errors (right) of experiments using soft manipulator in free environments, with (a) two points and (b) DEP-BTA (44) as shape features.

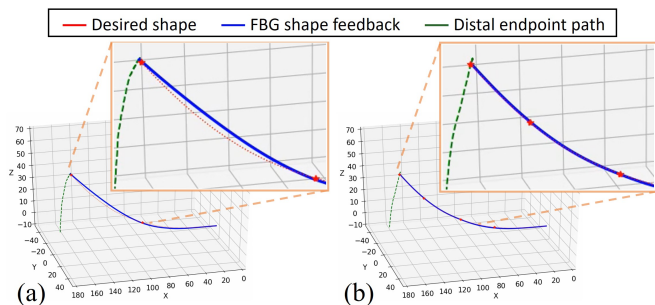


Fig. 9: Final shapes of experiments using soft manipulator with (a) two points and (b) DEP-BTA as shape descriptions.

are different in all experiments, where the desired endpoint position is outside the initial workspace. The asymptotic convergences of shape errors in Fig. 8 show that the robot's 3-D shape described by two features can be controlled to the desired configurations. We are noticed that the final shape described by two points (42) is slightly different from the desired one as shown in Fig. 9 (a), where the distal section is nearly stretched to a straight line, while that described by DEP-BTA (44) involving distal endpoint positioning and deflections of two sections, imposes a desired configuration in Fig. 9 (b).

B. Shape Servoing Tasks in Unstructured Environments

These experiments were performed using two continuum robots in unstructured environments, and their typical snapshots are shown in Fig. 10. The results are accordingly presented in Fig. 11 and 12, respectively.

1) *Experiments using robotic-assisted colonoscope system in unstructured environments:* The experiments using the colonoscope system were conducted in four different unstructured environments, including the tests with a rigid rod, 100 g payload, foam, and a soft bag filled with water, as illustrated in Fig. 10 (a), (b), (c), and (d), respectively, and the results are presented in Fig. 11 (a), (b), (c), and (d). We constructed two points (42) and bending/twist angles (43) to describe the

shape of distal continuum mechanism of the colonoscope. For brevity in this presentation, the experimental results using two points (42) can be referred to the attached video.

Fig. 11 (a) indicates the results of the first experiment in collisions with a rigid rod, during which we performed three random collisions to the distal part of colonoscope using the rod as unexpected external disturbances. Note that CPDE showing obvious perturbations in the left image is plotted by gradient colors, aiming to avoid overlap of back and forth curves when using the same color, so as to intuitively depict the experiment outcomes. Apart from this, the green and red points here represent the starting and desired points, respectively. Meanwhile, we can observe the sudden increases of the shape error e corresponding to the feature x (43) in the right figure, as well as the estimation errors, where the pink lines represent the time instants when encountering the collisions. It is worth observing that the errors can keep converging after each collision, which is contributed by both the robustness of shape flow predictor and controller, as well as the adaptability of NNs approximation with the weights tuning procedure. The results prove that our method can online update the time-varying model and servo-control the shape towards the desired one despite intense and sharp perturbations.

We then evaluated the algorithm by applying a mass of 100 g weight that can be treated as extra unknown payload on the tip of continuum mechanism as shown in Fig. 10 (b). The initial shape of continuum mechanism suffers an unexpected and obvious deformation under this payload as compared with other initial configurations in Fig. 10. The results in Fig. 11 (b) illustrate that CPDE can approach the desired point, and all the shape control and estimation errors are asymptotically minimized to zeros, thus prove that our method can estimate the model of continuum mechanism under unknown payload and simultaneously impose the desired 3-D shape.

The third experiment was performed with collision between the robot tip and an elastic foam as shown in Fig. 10 (c), which mimics interacting with elastic tissues during surgery. Note that the continuum mechanism was not in contact with the foam initially. Therefore, the mechanism's model after the collision is considered as different from that updated in free space before, which becomes invalid during the interaction. The left plot of Fig. 11 (c) depicts the resulting CPDE, and the right plots illustrate the asymptotic minimization of shape errors. The twist error $|\Delta\kappa|$ is minimized to 0.783° at 1.2 s and then increases to a local maximum of 4.902° , while the bending error $|\Delta\varphi|$ still shows convergence. Such results are led by a modeling change of the mechanism after the collision together with an unknown external elastic force acting on the mechanism, yet the proposed NN-based controller can adaptively learn the changing model. With the model adaptation after encountering the foam, both errors continue to converge to zeros at approximately 4 s.

In the fourth experiment, a soft bag filled with water hangs over the continuum mechanism as shown in Fig. 10 (d) and has 340 g weight. The distal part of approximately 50 mm length was in contact with the bag regarded as a soft tissue and lifted it. Unlike the setups of deformable object manipulation [69], [70], the distal endpoint was not fixed with the soft bag.

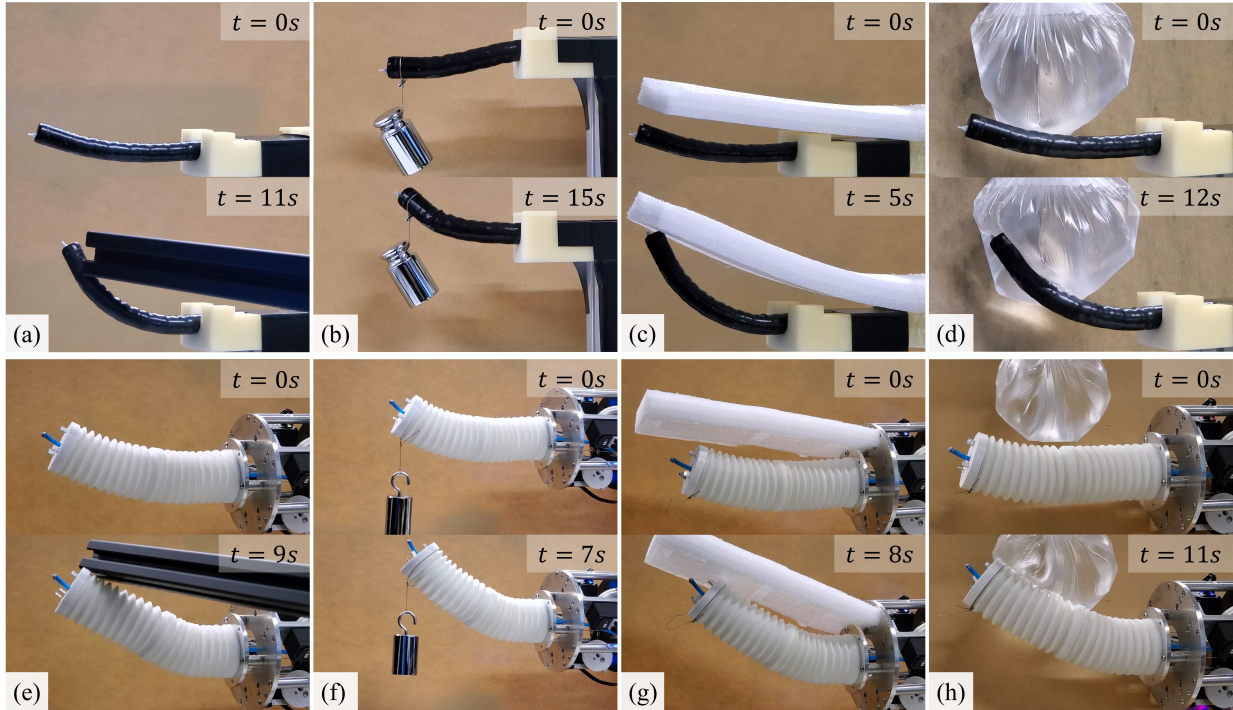


Fig. 10: Illustrations of unstructured environments in the tasks using colonoscope system and soft manipulator under (b) 100 g/(f) 200 g payload, and in collisions with (a)/(e) a rigid rod, (c)/(g) elastic foam, and (d)/(h) a soft bag filled with water.

It is concerned difficult to obtain a priori accurate model of continuum robot in this scenario since multiple factors that can affect the robot's behavior have to be considered (e.g., payloads and frictions). CPDE and asymptotic convergences of shape errors using the proposed approach are shown in Fig. 11 (d). The top-right plot demonstrates that the twist error $|\Delta\kappa|$ firstly converges to 0.368° at 2 s and then overshoots to 4.428° at 5 s, while the bending error $|\Delta\varphi|$ keeps asymptotic convergence to zero. After the collision, both κ and φ impose the desired values. From the results of these experiments, the proposed algorithm can online estimate the time-varying behavior of continuum robot, adaptively perform compliance to unstructured environments, and simultaneously servo-control the robot approaching the desired shape.

2) *Experiments using multi-section extensible soft manipulator in unstructured environments*: The proposed algorithm was also evaluated on the soft manipulator in four unstructured environments, including the tasks with a rigid rod, 200 g payload, foam, and a soft bag filled with water, as shown in Fig. 10 (e), (f), (g), and (h), respectively. Two points (42) and DEP-BTA (44) were used for shape descriptions. The results using DEP-BTA (44) are accordingly presented in Fig. 12, and those using two points (42) are recorded in the video. Note that the lengths of initial and desired configurations are different in all experiments, during which the robot has to be extended to impose the desired shape.

During the first experiment, three random collisions were created from the rigid rod as shown in Fig. 10 (e). In the right plots of Fig. 12 (a), the collisions brought sudden increases to the shape errors, and the time instants when encountering the collisions are represented by pink lines. In the left image, we can observe the corresponding perturbations of CPDE plotted

by gradient colors. The distal endpoint is servo-controlled to the desired location after the collisions, and the shape errors demonstrate minimization to zeros, indicating the robustness and adaptability of our method against external disturbances.

In the second test, the proposed algorithm was evaluated under unknown payload as shown in Fig. 10 (f), where a mass of 200 g weight was attached to the distal endpoint of soft manipulator. Fig. 12 (b) demonstrates the asymptotic convergences of resulting CPDE and shape errors. The errors exhibit adaptive adjustment in the local region near the desired shape as depicted in the left image. These results on a different soft robot prove that our method is generic and can adaptively identify the robot model in the presence of unknown payload, and control the robot into target configuration.

The third experiment was performed in collision with the elastic foam as shown in Fig. 10 (g). As previously mentioned, the robot in the initial configuration did not interact with the foam until it was bent to a certain angle, hence there was a difference in its models before and after the collision. The left plot of Fig. 12 (c) shows that CPDE outputs a smooth path in free space, and it approaches the desired configuration by using our adaptive NNs that can online approximate the interaction model after the collision. Such performance is also quantitatively illustrated in the right images, where the shape errors are asymptotically minimized to zeros with the adaptation to unknown external conditions.

In the fourth task, a soft bag filled with water of 340 g weight hangs on the soft manipulator as shown in Fig. 10 (h). The robot has to lift the soft object and move to the desired configuration, and it is hard to acquire a priori accurate model in such environment. The resulting CPDE and asymptotic convergences of shape errors to zeros in

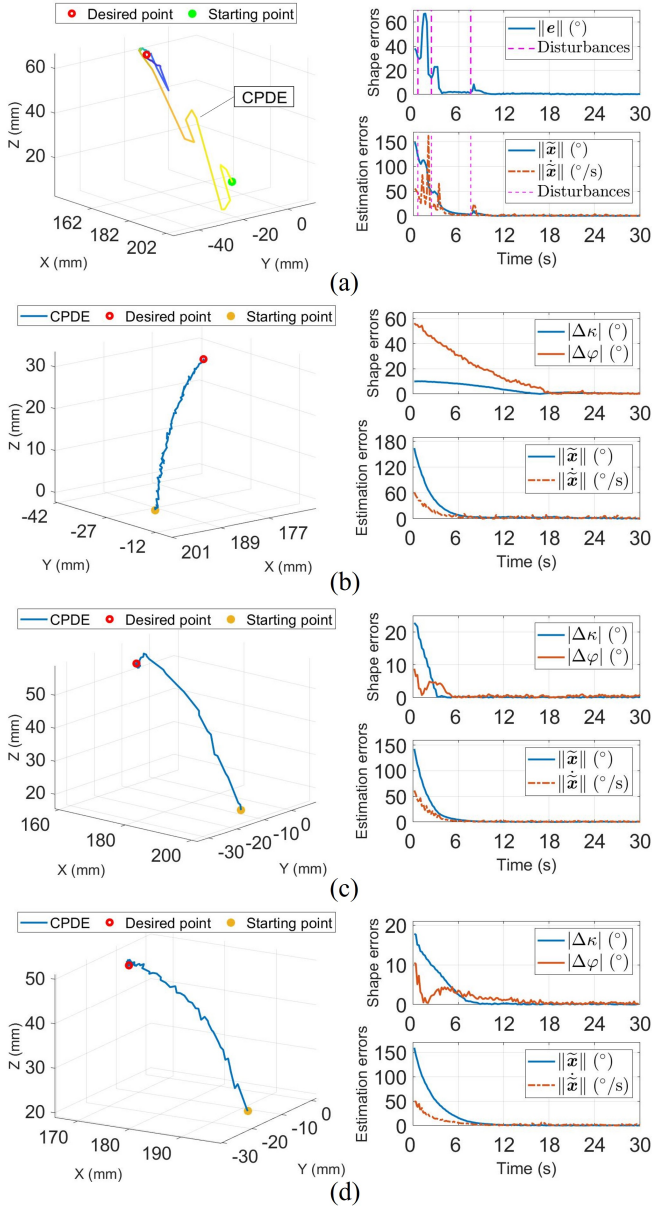


Fig. 11: CPDE (left) and shape errors (right) of experiments using colonoscope system in unstructured environments, including the tests with (a) a rigid rod, (b) 100 g payload, (c) foam, and (d) a soft bag filled with water.

Fig. 12 (d) indicate similar behaviors with those using the colonoscope system. Specifically, the shape errors decrease rapidly in free space, and then converge to zeros after the interaction, which is contributed by the fast adaptation to unknown disturbances under the proposed controller. These results demonstrate that our algorithm can online learn the model of continuum robot, adaptively conform to unstructured environments, and simultaneously impose the desired shape.

C. Shape Servoing Tasks for Special Validations

In these tasks, we performed shape servoing tasks to further validate the proposed method, including effectiveness of NNs approximation, performance when using longer soft manipulator, and performance when with unreachable desired shape.

1) *Effectiveness of NNs Approximation*: To prove that the proposed algorithm is able to learn the rows of combined Ja-

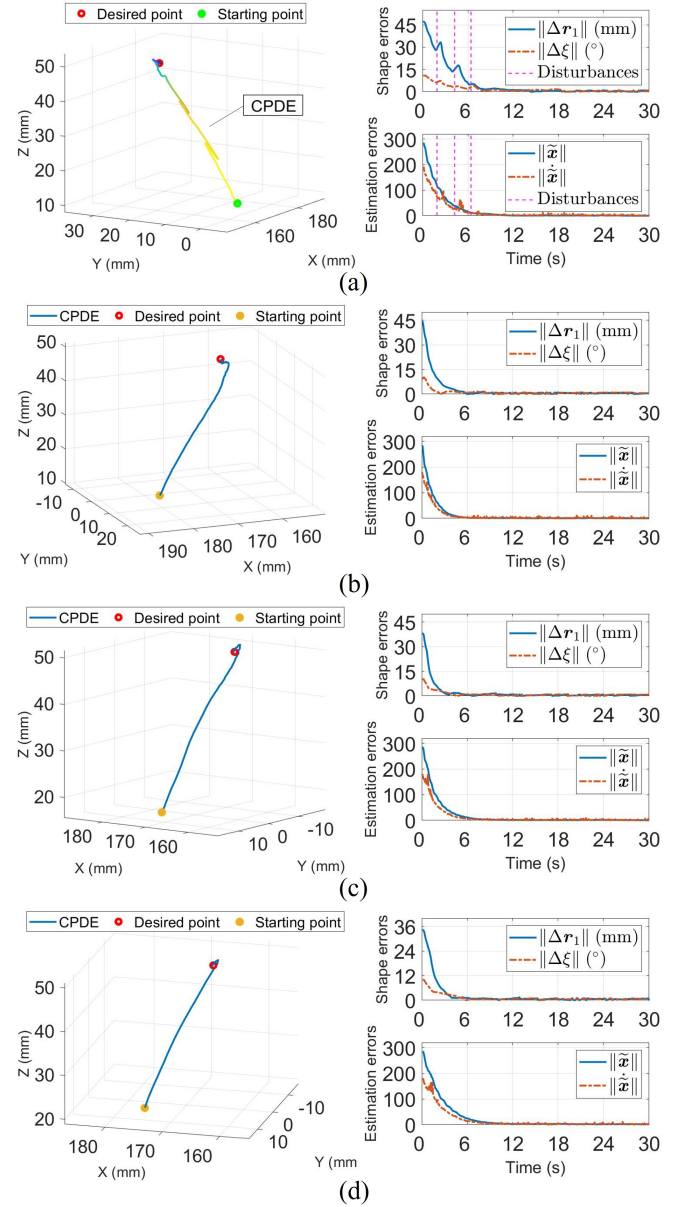


Fig. 12: CPDE (left) and shape errors (right) of experiments using soft manipulator in unstructured environments, including the tests with (a) a rigid rod, (b) 200 g payload, (c) foam, and (d) a soft bag filled with water.

cobian $J_c(q)$, five shape servoing tasks using the colonoscope system in free environments were performed, and each task was repeated four times. After the first experiment of each task, the afterward experiments were repeated and started by utilizing the weight matrices \widehat{W}_i , $i \in \{1, 2, \dots, m\}$, updated from the previous completion rather than those obtained from normalized initialization. The results are illustrated in Fig. 13 (a), and the average convergence time (in terms of repeated times) of five tasks are recorded in Table I. Note that during each task, the robot's shape was controlled to the same initial configuration after each completion, the processes of which are indicated by the white gaps in the top-right plot, while those of the repeated experiments are accordingly marked and presented in the shade.

From the average time in Table I as well as the asymptotic

TABLE I: Average convergence time (s) of experiments to validate the effectiveness of NNs approximation

Repeat times	1	2	3	4
Average time (s)	15.33	11.00	11.40	10.87

convergences of shape errors in the the top-right plot of Fig. 13 (a), it can be noticed that the latter three convergences are faster than the first one (by around 28.25% in average) during each task and they take a similar amount of time. Meanwhile, the distal endpoint has similar paths during the latter few convergences as shown in the left image, and there are few increases in the estimation errors in the bottom-right plot. These results prove that the proposed shape flow predictor (11) together with the composite adaptation law (25) have updated the weight matrices to steady values after the first attempt, and the learned Jacobian during the afterward repeated experiments only depends on the robot configuration \mathbf{q} .

2) *Validation for Unreachable Desired Shape*: An experiment using the colonoscope system with an unreachable desired shape was conducted to evaluate the performance of our method in such circumstance, where the desired position of distal endpoint is outside its workspace as shown in Fig. 14. CPDE and shape errors are depicted in the left and right images of Fig. 13 (b), respectively, from which we can observe a steady-state error in the 2-norm of position error of distal endpoint $\|\Delta \mathbf{r}_{e1}\|$ since its desired position is not feasible. Although the distal endpoint cannot be controlled to the desired position, the right plot of Fig. 14 demonstrates that the shape of distal continuum mechanism can still approach the desired one by using the proposed algorithm.

3) *Validation on Longer Continuum Robot*: This experiment was performed using a soft continuum manipulator newly designed with two longer sections, the length of which was increased from 180 mm to 298 mm as shown in Fig. 6, and 90 FBG-sections in the fiber were accordingly utilized for 3-D shape sensing and feedback. Due to the variable length of soft manipulator, its initial and desired lengths are different in this experiment. Fig. 13 (c) demonstrates the resulting CPDE and the asymptotic convergences of shape errors described by two points (42), showing that the proposed algorithm is generic and feasible for longer continuum robot. The validation on another longer robot can refer to the afterward phantom experiment using the colonoscope system with 400 mm length.

D. Shape Servoing Tasks for Methods Comparison

The interactions with various obstacles and inherent uncertainties of continuum robot can negatively affect the modeling of its deformation behavior. Accordingly, a priori knowledge of the modeling is considered as inaccurate and invalid in unstructured environments. We conducted four tasks to compare the performance of our proposed learning-based approach with two model-based methods using a fixed model and a constant curvature model, respectively. By deploying the colonoscope system with bending/twist angles (43) as shape feature, the first two experiments were compared with a controller using a constant combined Jacobian $\hat{\mathbf{J}}_c(\mathbf{q})$ estimated around the starting point in free space, the purpose of which is to compare with a method that only utilizes a fixed model [69]. For

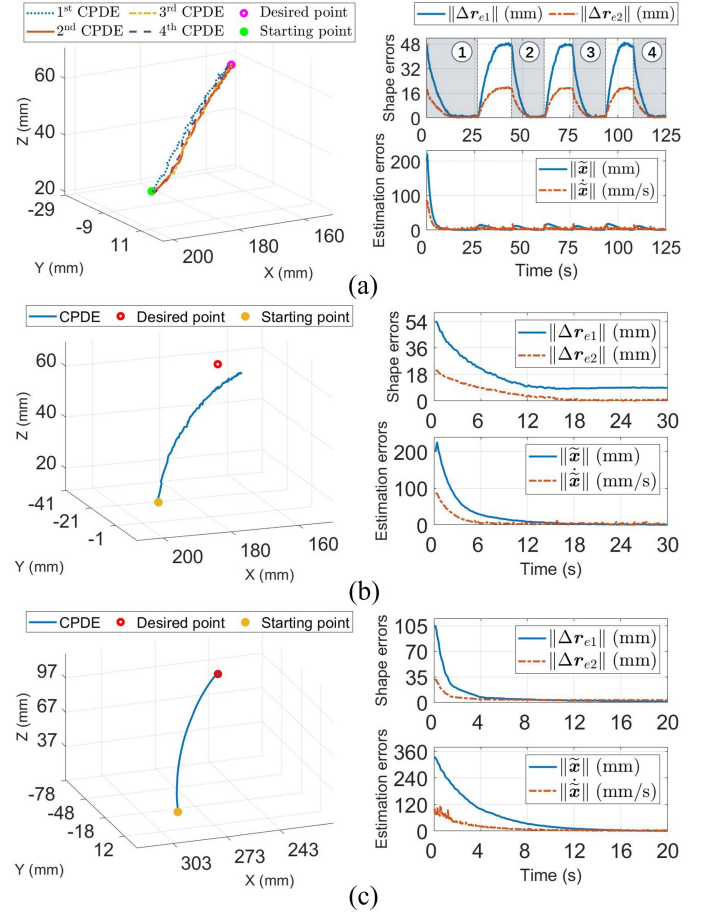


Fig. 13: CPDE (left) and shape errors (right) of experiments for spacial validations: (a) effectiveness of NNs approximation, (b) validation for unreachable desired shape, and (c) validation on longer soft continuum manipulator.

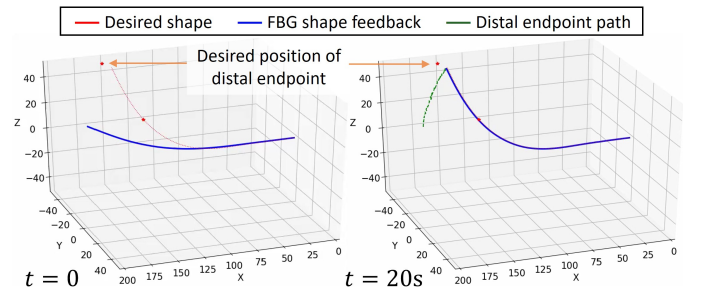


Fig. 14: Snapshots of initial (left) and final (right) FBG shapes in the experiment when the desired shape is not feasible.

brevity of presentation, the results of these two experiments can be found in the supplementary video, where the fixed-model method demonstrates oscillation even divergence, while ours shows asymptotic convergences and robustness against internal uncertainties as well as external perturbations.

The next two experiments were performed by comparing our controller with another one using a constant curvature model [5], where the robot shape was described by two points (42). The first test was conducted by introducing internal uncertainties, and the second one was with internal uncertainties and exogenous disturbances. Two methods were quantitatively compared according to the metrics of CPDE, shape control errors $\|e\|$, and estimation errors $\|\tilde{\mathbf{x}}\|$, which are

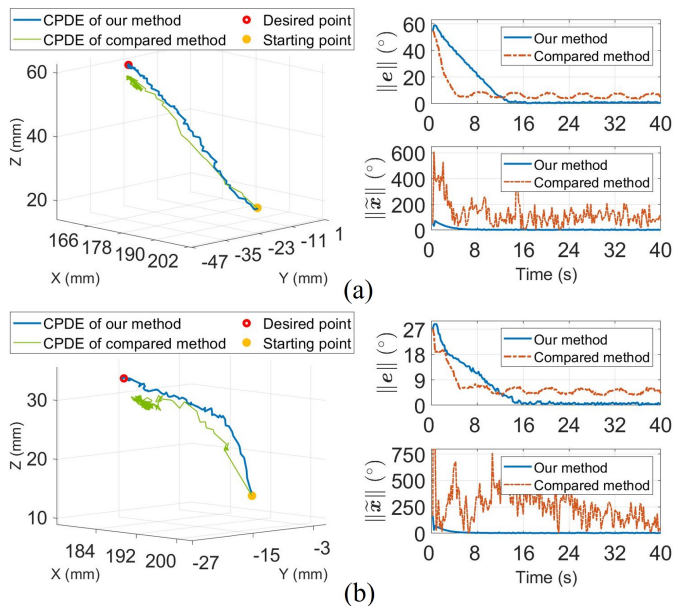


Fig. 15: CPDE (left), and shape control and estimation errors (right) of experiments compared with model-based method using constant curvature with (a) internal uncertainties and (b) external disturbances in addition.

presented in Fig. 15. In the left plots, the blue and green curves represent the endpoint paths using our method and model-based method, respectively, and the yellow and red points are denoted as the starting and desired locations. In the right plots, the shape errors using our method and model-based method are accordingly represented by blue and red curves.

1) *Experiment with Internal Uncertainties*: To ensure the same conditions of comparison experiments, the first experiment was performed by injecting the same unknown uncertainties into the actuator input \dot{q} , i.e., the actual actuator velocity applied to the robot has significant deviations from the command one. As shown in the left image of Fig. 15 (a) demonstrating CPDE, the distal endpoint controlled by the model-based method without modeling the uncertainties oscillates in a region, while ours can automatically approach the desired position, which is contributed by our adaptive NNs approximation to the time-varying model with unknown uncertainties. The right plots show that although the shape control error using the model-based method converges faster around the starting point than ours, its shape is not controlled to the desired one but demonstrate oscillations around it after 5.6 s. Our algorithm initially costs a few more iterations for adaption to the uncertainties, while the error shows asymptotic minimization to zeros at 11.2 s. Moreover, since the model-based method did not update the robot model, its estimation error is not convergent as compared with ours, but shows random vibrations.

2) *Experiment with Internal Uncertainties and External Disturbances*: In addition to the unknown actuation uncertainties, we conducted the second test in a constrained environment with the soft bag filled with water as depicted in Fig. 10 (d), during which the same conditions were guaranteed when using both methods. As noticed in the right plots of Fig. 15 (b), the shape control error using the model-based

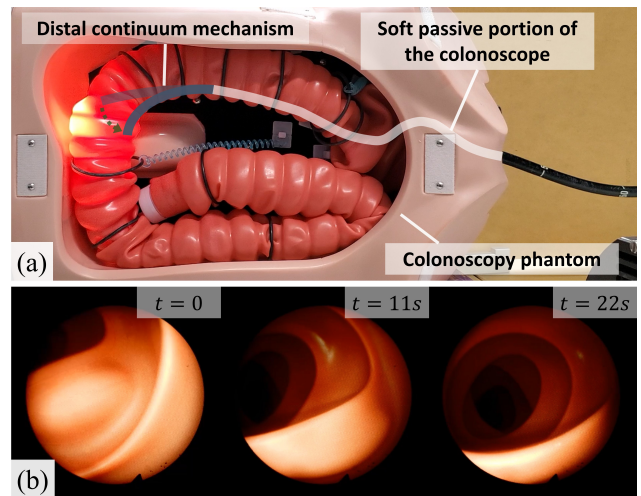


Fig. 16: (a) Task setup of shape control for robotic colonoscopy, and (b) snapshots of endoscopic views.

method does not show regulation but oscillates around a large value after the collision, while that using our approach together with the estimation error show the asymptotic convergences to zeros in such scenario. This can be also indicated by CPDE in the left image, where CPDE controlled by the model-based method oscillates in a region far from the desired configuration. Although it is difficult for a priori knowledge of the robot model to be effective and accurate when considering the internal uncertainties and external perturbations, from the above results with these unexpected conditions, we can confirm that the proposed adaptive NN controller can online update the unknown model of the continuum robot and robustly drive its 3-D shape towards the desired configuration.

E. Case Studies in Medical Contexts

In this section, two case studies were performed including shape control for robotic colonoscopy and oropharyngeal (OP) swab sampling. The experimental setups and snapshots are illustrated in Fig. 16 and 17, respectively, and the results are accordingly shown in Fig. 18 (a) and (b).

1) *Shape Control for Robotic Colonoscopy*: We deployed the colonoscope with 400 mm length inside a colonoscopy phantom (Kyoto Kagaku M40), and used the proposed method to automatically control the shape of its distal continuum mechanism. The setup is shown in Fig. 16 (a), where the distal continuum mechanism at the corner has to bend downwards to acquire a better endoscopic view for insertion guidance. Fig. 16 (b) presents the snapshots of endoscopic views, from which we can observe that the view in this task was controlled from an unclear one to a feasible one for continuing insertion. Note that the colonoscope has a soft passive portion with 280 mm length inside the phantom, which was not fixed and could collide with the phantom frequently resulting in unknown disturbances to the system. Due to these intense environmental perturbations, CPDE and shape control error $\|e\|$ described by two points (42) behave some oscillations as depicted in the left and right plots of Fig. 18 (a), respectively, while their convergences show that our algorithm can adaptively update the time-varying model of continuum robot and simultaneously

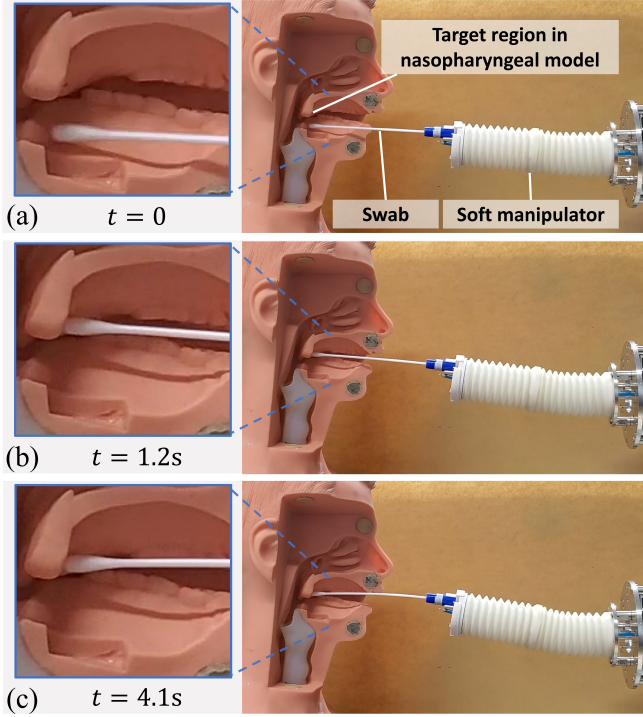


Fig. 17: Snapshots of OP swab sampling: (a) initial setup, (b) interaction with target, and (c) shape control completion.

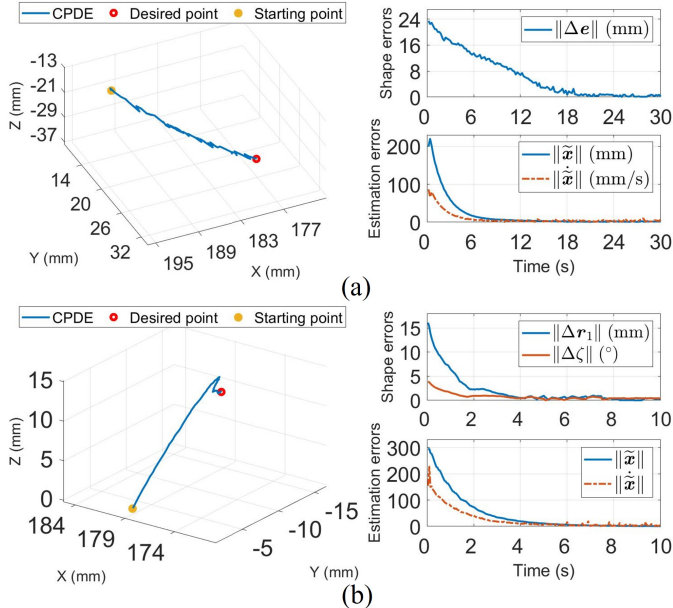


Fig. 18: CPDE (left) and shape errors (right) of case studies in medical scenarios: (a) shape control in robotic colonoscopy, and (b) OP swab sampling.

servo-control it to the desired shape against unknown external disturbances during robotic colonoscopy.

2) *OP Swab Sampling*: The setup of this task is illustrated in Fig. 17, where a swab is attached to the distal endpoint of the soft manipulator and the swab tip has to interact with the target region of a nasopharyngeal model (KJR/7208) for successful sampling. The swab is deformed by the interaction as shown in Fig. 17 (b) and (c), and the robot model during the interaction is regarded as different from the initial one. The left image of Fig. 18 (b) demonstrates the resulting CPDE,

and the right plots show the asymptotic minimization of shape errors described by DEP-BTA (44). The position error of distal endpoint $\|\Delta r_1\|$ behaves slower convergence after the collision between the swab tip and the target, yet the algorithm adaptively keeps the errors converging to zeros near the desired configuration. These results of phantom experiments prove that our controller can perform robust compliance to the deformable environments, online learning of the time-varying model, and simultaneously control the 3-D shape of continuum robot into the desired one in these credible contexts.

F. Discussion and Limitation of the Method

Apart from CPDE and shape errors presented in the figures above, the ranks of matrix $\hat{J}_c(q)\hat{J}_c^+(q)$ using the proposed algorithm were recorded and did not reduce during the experiments, and the control inputs \dot{q} from (26) did not reach the threshold, thus preventing fast motions of the robot. From all these results using two different continuum robots, we can notice that the proposed control method can robustly and adaptively control the 3-D shape of the continuum robot without any priori model in various unstructured environments. As for the soft manipulator featured with variable stiffness and length, DEP-BTA composed of distal endpoint positioning as well as bending/twisting of each extensible section, is better to describe and control its shape, rather than the feature of two points which may bring unexpected extension/compression to the soft sections (e.g., the distal section was stretched in Section V - A, and others in Section V - B - 2) illustrated in the attached video). The limitation of the approach is that the deployed FBG shape sensing does not consider the variable arc length of the soft manipulator, though we can approximate and control its time-varying length by positioning its distal endpoint. We will enable an accurate length estimation using FBG sensors to further cope with this issue. With an additional structure to be designed and integrated in our future work, the performance of controlling the robot with variable length will be improved. 3-D shape control of continuum robot with more sections will also be investigated.

VI. CONCLUSION

In this work, we propose a novel and generic data-driven approach for adaptive 3-D shape control of surgical continuum robots using FBG shape feedback in unstructured environments. An enhanced multi-core FBGs-equipped method with an accurate shape sensing algorithm is employed to obtain the robot's shape feedback without external sensing units; thus, it can be utilized in MIS with occlusions of sight-of-view. The proposed algorithm enables robust model learning of the continuum robot and simultaneous servo-control of the robot imposing the desired shape without any priori knowledge by leveraging the nonlinear NNs approximation, thereby facilitating its applications with highly nonlinear uncertainties and unknown environmental interactions. A NN-based shape flow predictor together with a composite adaptation law are introduced for asymptotic regulations of shape estimation errors and online update of the NN weights. The stability of the close-loop system using our adaptive NN controller has been theoretically proved by Lyapunov theory.

To evaluate the performance of the proposed method in real applications, a comprehensive and detailed experimental study has been conducted using two different continuum robots, including the distal continuum mechanism of the robotic-assisted colonoscope system and the multi-section extensible soft manipulators, both equipped with multi-core FBG fibers for 3-D shape sensing. It is worth noting that the soft manipulator is featured with variable length and stiffness. The results that consist of the converging paths of the distal endpoint and the asymptotic regulation of the shape control and estimation errors to zeros, demonstrate the versatility, adaptability, and superiority of our method in various unstructured environments and phantom experiments against unexpected external disturbances, which facilitate its practical deployments to various continuum robots and flexible instruments.

Although we evaluate the performance of our method in 3-D Cartesian space, we only test it with desired configurations in C-shape and those described in S-shape are not validated, which will be investigated using an improved soft robot in the future. Since the variable length of the soft manipulator would affect the performance, a key issue is to acquire the accurate sensing length of the robot [10]. For this purpose, an assisting device and methodology using FBG sensors will be designed, validated, and reported later. For future research, due to the versatility of the proposed controller, it can be extended for more practical tasks, such as soft tissue manipulation [69], [70], and eye-in-hand visual servoing [9], [20], [51]. The control method will also be introduced in an energy-based planning algorithm for underactuated manipulation of continuum robots [37] by utilizing the differences in curvatures/twists between consecutive FBG-sections. We will further investigate advanced nonlinear observers and control approaches for dynamic systems within efficient and safe frameworks to improve the performance of 3-D shape servoing for continuum robots.

APPENDIX A

3-D SHAPE SERVOING ALGORITHM

Algorithm 1: 3-D shape servoing algorithm

Initialization:
1 $\mathbf{x}_d \leftarrow$ define a shape description and a desired shape
2 $\epsilon_e \leftarrow$ specify a positive scalar as threshold
3 $\widehat{\mathbf{W}}_i, i \in \{1, 2, \dots, m\} \leftarrow$ initialize NN weight matrices
Shape servoing:
4 **while** shape error norm $\|e\| > \epsilon_e$ **do**
5 $\hat{\mathbf{x}}, \tilde{\mathbf{x}} \leftarrow$ predict shape flow (11) and its error (13)
6 $\tilde{\mathbf{x}} \leftarrow$ compute shape estimation error (12)
7 $\mathbf{q} \leftarrow$ measure actuator position
8 $\widehat{\mathbf{W}} \leftarrow$ update vector of NN weights (25)
9 $\widehat{\mathbf{J}}_c(\mathbf{q}) \leftarrow$ compute combined Jacobian matrix (10)
10 $\dot{\mathbf{q}} \leftarrow$ compute velocity controller (26)
11 Command actuator motion $\dot{\mathbf{q}}$
12 $\mathbf{r}, \mathbf{x} \leftarrow$ generate 3-D shape from FBG-measured points
13 $e \leftarrow$ calculate shape control error
14 **end**

APPENDIX B

PROOF OF POSITIVE SEMI-DEFINITENESS OF $\mathcal{R}(t)$ IN (30)

Recall that the auxiliary function $\mathcal{H}(t)$ is generated by

$$\dot{\mathcal{H}} = \mathbf{r}_x^\top (\boldsymbol{\delta} - \beta_x \text{sat}(\tilde{\mathbf{x}})) \quad (45)$$

By integrating $\dot{\mathcal{H}}$ and substituting $\mathbf{r}_x = \dot{\tilde{\mathbf{x}}} + \alpha_x \tilde{\mathbf{x}}$ in (24), it is obtained that

$$\begin{aligned} \mathcal{H}(t) &= \mathcal{H}(0) + \int_0^t \mathbf{r}_x^\top (\boldsymbol{\delta} - \beta_x \text{sat}(\tilde{\mathbf{x}})) d\tau \\ &= \mathcal{H}(0) + \int_0^t (\dot{\tilde{\mathbf{x}}} + \alpha_x \tilde{\mathbf{x}})^\top (\boldsymbol{\delta} - \beta_x \text{sat}(\tilde{\mathbf{x}})) d\tau \\ &= \mathcal{H}(0) + \int_0^t \tilde{\mathbf{x}}^\top \boldsymbol{\delta} d\tau - \int_0^t \beta_x \tilde{\mathbf{x}}^\top \text{sat}(\tilde{\mathbf{x}}) d\tau \\ &\quad + \int_0^t \alpha_x \tilde{\mathbf{x}}^\top (\boldsymbol{\delta} - \beta_x \text{sat}(\tilde{\mathbf{x}})) d\tau \end{aligned} \quad (46)$$

The second and third integrals can be transformed as

$$\begin{aligned} \mathcal{H}(t) &= \mathcal{H}(0) + \tilde{\mathbf{x}}^\top \boldsymbol{\delta} - \tilde{\mathbf{x}}^\top(0) \boldsymbol{\delta}(0) - \int_0^t \tilde{\mathbf{x}}^\top \dot{\boldsymbol{\delta}} d\tau \\ &\quad - \beta_x \sum_{i=1}^m |\tilde{\mathbf{x}}_i(t)| + \beta_x \sum_{i=1}^m |\tilde{\mathbf{x}}_i(0)| \\ &\quad + \int_0^t \alpha_x \tilde{\mathbf{x}}^\top (\boldsymbol{\delta} - \beta_x \text{sat}(\tilde{\mathbf{x}})) d\tau \end{aligned} \quad (47)$$

Since $\sum_{i=1}^m |\tilde{\mathbf{x}}_i(t)| \geq \|\tilde{\mathbf{x}}\|$, taking the upper bound of above equation yields

$$\begin{aligned} \mathcal{H}(t) &\leq \mathcal{H}(0) + \|\tilde{\mathbf{x}}\| \|\boldsymbol{\delta}\| - \tilde{\mathbf{x}}^\top(0) \boldsymbol{\delta}(0) \\ &\quad + \int_0^t \|\tilde{\mathbf{x}}\| \|\dot{\boldsymbol{\delta}}\| d\tau - \beta_x \|\tilde{\mathbf{x}}\| + \beta_x \sum_{i=1}^m |\tilde{\mathbf{x}}_i(0)| \\ &\quad + \int_0^t \alpha_x \|\tilde{\mathbf{x}}\| \|\boldsymbol{\delta} - \beta_x \text{sat}(\tilde{\mathbf{x}})\| d\tau \end{aligned} \quad (48)$$

Substituting the upper bounds of $\boldsymbol{\delta}$ and $\dot{\boldsymbol{\delta}}$ from (9), we can obtain that

$$\begin{aligned} \mathcal{H}(t) &\leq \mathcal{H}(0) - \tilde{\mathbf{x}}^\top(0) \boldsymbol{\delta}(0) + \beta_x \sum_{i=1}^m |\tilde{\mathbf{x}}_i(0)| \\ &\quad - (\beta_x - b_{\delta 1}) \|\tilde{\mathbf{x}}\| \\ &\quad - \int_0^t \alpha_x \left(\beta_x - b_{\delta 1} - \frac{b_{\delta 2}}{\alpha_x} \right) \|\tilde{\mathbf{x}}\| d\tau \end{aligned} \quad (49)$$

We can conclude that the last two terms on the right of the above inequality both negative semi-definite if the condition

$$\beta_x \geq b_{\delta 1} + \frac{b_{\delta 2}}{\alpha_x} \quad (50)$$

in (28) is satisfied, then we further have

$$\mathcal{H}(t) \leq \mathcal{H}(0) - \tilde{\mathbf{x}}^\top(0) \boldsymbol{\delta}(0) + \beta_x \sum_{i=1}^m |\tilde{\mathbf{x}}_i(0)| \quad (51)$$

and prove $\mathcal{R}(t) \geq 0$ in (30).

APPENDIX C

NN PARAMETERS IN THE EXPERIMENTS

In the experiments using the colonoscope system, the basis of center values $\boldsymbol{\mu}_{0j} \in \mathbb{R}^2$ and that of width values σ_{0j} , $j \in \{1, 2, \dots, 9\}$, are listed in Table II and III, respectively. The center values $\boldsymbol{\mu}_{ij} \in \mathbb{R}^2$ of the i -th NN and the corresponding width values σ_{ij} , $i \in \{1, 2\}$, were initialized by sorting the columns of the basis $\boldsymbol{\mu}_{0j}$ and σ_{0j} in random orders.

TABLE II: The basis of center values $\boldsymbol{\mu}_{0j}$ of the j -th neuron

j	1	2	3	4	5	6	7	8	9
Basis	1200	1200	1800	1800	3000	3000	3600	3600	2400
elements	800	3200	1400	2600	2600	1400	800	3200	2000

TABLE III: The basis of width values σ_{0j} of the j -th neuron

j	1	2	3	4	5	6	7	8	9
σ_{0j}	200	200	600	600	600	600	200	200	600

In the same way as above, the center values $\mu_{ij} \in \mathbb{R}^6$ and the corresponding width values σ_{ij} , $i \in \{1, 2, \dots, 6\}$ in the other experiments using the soft manipulator, were initialized by randomly sorting the columns of the basis of center values μ_{0j} and those of width values σ_{0j} , $j \in \{1, 2, \dots, 13\}$, listed in Table IV and V, respectively.

TABLE IV: The basis of center values μ_{0j} of the j -th neuron

j	1	2	3	4	5	6	7	8	9	10	11	12	13
Basis elements	100	500	100	100	300	100	100	500	100	500	300	100	300
	100	100	500	100	100	300	100	500	500	100	300	300	100
	100	100	100	500	100	100	300	100	500	500	100	300	300
	800	500	800	800	650	800	800	500	800	500	650	800	650
	800	800	500	800	800	650	800	500	500	800	650	650	800
	800	800	800	500	800	800	650	800	500	500	800	650	650

TABLE V: The basis of width values σ_{0j} of the j -th neuron

j	1	2	3	4	5	6	7	8	9	10	11	12	13
σ_{0j}	200	200	200	200	500	500	500	200	200	200	500	500	500

REFERENCES

- [1] J. Burgner-Kahrs, D. C. Rucker, and H. Choset, "Continuum robots for medical applications: A survey," *IEEE Transactions on Robotics*, vol. 31, no. 6, pp. 1261–1280, 2015.
- [2] A. H. Gosline, N. V. Vasilyev, E. J. Butler, C. Folk, A. Cohen, R. Chen, N. Lang, P. J. Del Nido, and P. E. Dupont, "Percutaneous intracardiac beating-heart surgery using metal mems tissue approximation tools," *The International journal of robotics research*, vol. 31, no. 9, 2012.
- [3] R. E. Goldman, A. Bajo, and N. Simaan, "Compliant motion control for multisegment continuum robots with actuation force sensing," *IEEE Transactions on Robotics*, vol. 30, no. 4, pp. 890–902, 2014.
- [4] A. Bajo, R. E. Goldman, L. Wang, D. Fowler, and N. Simaan, "Integration and preliminary evaluation of an insertable robotic effectors platform for single port access surgery," in *2012 IEEE International Conference on Robotics and Automation*. IEEE, 2012, pp. 3381–3387.
- [5] R. J. Webster III and B. A. Jones, "Design and kinematic modeling of constant curvature continuum robots: A review," *The International Journal of Robotics Research*, vol. 29, no. 13, pp. 1661–1683, 2010.
- [6] C. Shi, X. Luo, P. Qi, T. Li, S. Song, Z. Najdovski, T. Fukuda, and H. Ren, "Shape sensing techniques for continuum robots in minimally invasive surgery: A survey," *IEEE Transactions on Biomedical Engineering*, vol. 64, no. 8, pp. 1665–1678, 2016.
- [7] T. George Thuruthel, Y. Ansari, E. Falotico, and C. Laschi, "Control strategies for soft robotic manipulators: A survey," *Soft robotics*, vol. 5, no. 2, pp. 149–163, 2018.
- [8] S. Sefati, R. Hegeman, I. Iordachita, R. H. Taylor, and M. Armand, "A dexterous robotic system for autonomous debridement of osteolytic bone lesions in confined spaces: Human cadaver studies," *IEEE Transactions on Robotics*, 2021.
- [9] G. Fang, M. C. K. Chow, J. D. L. Ho, Z. He, K. Wang, T. C. Ng, J. K. H. Tsoi, P.-L. Chan, H.-C. Chang, D. T.-M. Chan, Y.-h. Liu, F. C. Holsinger, J. Y.-K. Chan, and K.-W. Kwok, "Soft robotic manipulator for intraoperative mri-guided transoral laser microsurgery," *Science Robotics*, vol. 6, no. 57, 2021.
- [10] H. Wang, B. Yang, Y. Liu, W. Chen, X. Liang, and R. Pfeifer, "Visual servoing of soft robot manipulator in constrained environments with an adaptive controller," *IEEE/ASME Transactions on Mechatronics*, vol. 22, no. 1, pp. 41–50, 2016.
- [11] J. Till, V. Aloï, and C. Rucker, "Real-time dynamics of soft and continuum robots based on cosserat rod models," *The International Journal of Robotics Research*, vol. 38, no. 6, pp. 723–746, 2019.
- [12] A. Vandini, C. Bergeles, B. Glocker, P. Giataganas, and G.-Z. Yang, "Unified tracking and shape estimation for concentric tube robots," *IEEE Transactions on Robotics*, vol. 33, no. 4, pp. 901–915, 2017.
- [13] S. Elayaperumal, J. C. Plata, A. B. Holbrook, Y.-L. Park, K. B. Pauly, B. L. Daniel, and M. R. Cutkosky, "Autonomous real-time interventional scan plane control with a 3-d shape-sensing needle," *IEEE transactions on medical imaging*, vol. 33, no. 11, pp. 2128–2139, 2014.
- [14] A. M. Franz, T. Haidegger, W. Birkfellner, K. Cleary, T. M. Peters, and L. Maier-Hein, "Electromagnetic tracking in medicine—a review of technology, validation, and applications," *IEEE transactions on medical imaging*, vol. 33, no. 8, pp. 1702–1725, 2014.
- [15] R. J. Roesthuis, M. Kemp, J. J. van den Dobbelsteen, and S. Misra, "Three-dimensional needle shape reconstruction using an array of fiber bragg grating sensors," *IEEE/ASME transactions on mechatronics*, vol. 19, no. 4, pp. 1115–1126, 2013.
- [16] F. Monet, S. Sefati, P. Lorre, A. Poiffaut, S. Kadoury, M. Armand, I. Iordachita, and R. Kashyap, "High-resolution optical fiber shape sensing of continuum robots: A comparative study," in *IEEE International Conference on Robotics and Automation (ICRA)*. IEEE, 2020.
- [17] Y. Chitalia, N. J. Deaton, S. Jeong, N. Rahman, and J. P. Desai, "Towards fbg-based shape sensing for micro-scale and meso-scale continuum robots with large deflection," *IEEE robotics and automation letters*, vol. 5, no. 2, pp. 1712–1719, 2020.
- [18] A. Denasi, F. Khan, K. J. Boskma, M. Kaya, C. Hennersperger, R. Göbl, M. Tirindelli, N. Navab, and S. Misra, "An observer-based fusion method using multicore optical shape sensors and ultrasound images for magnetically-actuated catheters," in *2018 IEEE International Conference on Robotics and Automation (ICRA)*. IEEE, 2018.
- [19] F. Alambeigi, S. A. Pedram, J. L. Speyer, J. Rosen, I. Iordachita, R. H. Taylor, and M. Armand, "Scade: Simultaneous sensor calibration and deformation estimation of fbg-equipped unmodeled continuum manipulators," *IEEE Transactions on Robotics*, vol. 36, no. 1, 2019.
- [20] X. Wang, G. Fang, K. Wang, X. Xie, K.-H. Lee, J. D. Ho, W. L. Tang, J. Lam, and K.-W. Kwok, "Eye-in-hand visual servoing enhanced with sparse strain measurement for soft continuum robots," *IEEE Robotics and Automation Letters*, vol. 5, no. 2, pp. 2161–2168, 2020.
- [21] S. Sefati, C. Gao, I. Iordachita, R. H. Taylor, and M. Armand, "Data-driven shape sensing of a surgical continuum manipulator using an uncalibrated fiber bragg grating sensor," *IEEE Sensors Journal*, 2020.
- [22] Y. Lu, B. Lu, B. Li, H. Guo, and Y.-H. Liu, "Robust three-dimensional shape sensing for flexible endoscopic surgery using multi-core fbg sensors," *IEEE Robotics and Automation Letters*, vol. 6, no. 3, 2021.
- [23] F. Xu, H. Wang, Z. Liu, and W. Chen, "Adaptive visual servoing for an underwater soft robot considering refraction effects," *IEEE Transactions on Industrial Electronics*, vol. 67, no. 12, pp. 10575–10586, 2019.
- [24] F. Alambeigi, Z. Wang, Y.-H. Liu, R. H. Taylor, and M. Armand, "A versatile data-driven framework for model-independent control of continuum manipulators interacting with obstructed environments with unknown geometry and stiffness," *arXiv preprint:2005.01951*, 2020.
- [25] D. B. Camarillo, C. F. Milne, C. R. Carlson, M. R. Zinn, and J. K. Salisbury, "Mechanics modeling of tendon-driven continuum manipulators," *IEEE transactions on robotics*, vol. 24, no. 6, pp. 1262–1273, 2008.
- [26] D. C. Rucker, R. J. Webster III, G. S. Chirikjian, and N. J. Cowan, "Equilibrium conformations of concentric-tube continuum robots," *The International journal of robotics research*, vol. 29, no. 10, 2010.
- [27] I. A. Gravagne, C. D. Rahn, and I. D. Walker, "Large deflection dynamics and control for planar continuum robots," *IEEE/ASME transactions on mechatronics*, vol. 8, no. 2, pp. 299–307, 2003.
- [28] D. B. Camarillo, C. R. Carlson, and J. K. Salisbury, "Configuration tracking for continuum manipulators with coupled tendon drive," *IEEE Transactions on Robotics*, vol. 25, no. 4, pp. 798–808, 2009.
- [29] D. C. Rucker and R. J. Webster III, "Statics and dynamics of continuum robots with general tendon routing and external loading," *IEEE Transactions on Robotics*, vol. 27, no. 6, pp. 1033–1044, 2011.
- [30] C. G. Frazzelle, A. D. Kapadia, and I. D. Walker, "A nonlinear control strategy for extensible continuum robots," in *2018 IEEE International Conference on Robotics and Automation (ICRA)*. IEEE, 2018.
- [31] D. Braganza, D. M. Dawson, I. D. Walker, and N. Nath, "A neural network controller for continuum robots," *IEEE transactions on robotics*, vol. 23, no. 6, pp. 1270–1277, 2007.
- [32] V. Falkenhahn, A. Hildebrandt, R. Neumann, and O. Sawodny, "Dynamic control of the bionic handling assistant," *IEEE/ASME Transactions on Mechatronics*, vol. 22, no. 1, pp. 6–17, 2016.
- [33] C. Della Santina, M. Bianchi, G. Grioli, F. Angelini, M. Catalano, M. Garabini, and A. Bicchi, "Controlling soft robots: balancing feedback and feedforward elements," *IEEE Robotics & Automation Magazine*, vol. 24, no. 3, pp. 75–83, 2017.
- [34] N. Simaan, K. Xu, W. Wei, A. Kapoor, P. Kazanzides, R. Taylor, and P. Flint, "Design and integration of a telerobotic system for minimally invasive surgery of the throat," *The International journal of robotics research*, vol. 28, no. 9, pp. 1134–1153, 2009.
- [35] C. M. Best, M. T. Gillespie, P. Hyatt, L. Rupert, V. Sherrod, and M. D. Killpack, "A new soft robot control method: Using model predictive

- control for a pneumatically actuated humanoid," *IEEE Robotics & Automation Magazine*, vol. 23, no. 3, pp. 75–84, 2016.
- [36] M. Khadem, J. O'Neill, Z. Mitros, L. Da Cruz, and C. Bergeles, "Autonomous steering of concentric tube robots via nonlinear model predictive control," *IEEE Transactions on Robotics*, vol. 36, no. 5, pp. 1595–1602, 2020.
- [37] E. Franco and A. Garriga-Casanovas, "Energy-shaping control of soft continuum manipulators with in-plane disturbances," *The International Journal of Robotics Research*, vol. 40, no. 1, pp. 236–255, 2021.
- [38] D. Ross, M. P. Nemitz, and A. A. Stokes, "Controlling and simulating soft robotic systems: insights from a thermodynamic perspective," *Soft Robotics*, vol. 3, no. 4, pp. 170–176, 2016.
- [39] D. C. Rucker, J. Das, H. B. Gilbert, P. J. Swaney, M. I. Miga, N. Sarkar, and R. J. Webster, "Sliding mode control of steerable needles," *IEEE Transactions on Robotics*, vol. 29, no. 5, pp. 1289–1299, 2013.
- [40] M. C. Yip and D. B. Camarillo, "Model-less feedback control of continuum manipulators in constrained environments," *IEEE Transactions on Robotics*, vol. 30, no. 4, pp. 880–889, 2014.
- [41] M. C. Yip and D. B. Camarillo, "Model-less hybrid position/force control: a minimalist approach for continuum manipulators in unknown, constrained environments," *IEEE Robotics and Automation Letters*, vol. 1, no. 2, pp. 844–851, 2016.
- [42] M. Li, R. Kang, D. T. Branson, and J. S. Dai, "Model-free control for continuum robots based on an adaptive kalman filter," *IEEE/ASME Transactions on Mechatronics*, vol. 23, no. 1, pp. 286–297, 2017.
- [43] F. Holsten, M. P. Engell-Nørregård, S. Darkner, and K. Erleben, "Data driven inverse kinematics of soft robots using local models," in *2019 International Conference on Robotics and Automation (ICRA)*. IEEE, 2019, pp. 6251–6257.
- [44] X. Wang, Y. Li, and K.-W. Kwok, "A survey for machine learning-based control of continuum robots," *Frontiers in Robotics and AI*, p. 280, 2021.
- [45] M. Rolf and J. J. Steil, "Efficient exploratory learning of inverse kinematics on a bionic elephant trunk," *IEEE transactions on neural networks and learning systems*, vol. 25, no. 6, pp. 1147–1160, 2013.
- [46] M. Giorelli, F. Renda, M. Calisti, A. Arienti, G. Ferri, and C. Laschi, "Neural network and jacobian method for solving the inverse statics of a cable-driven soft arm with nonconstant curvature," *IEEE Transactions on Robotics*, vol. 31, no. 4, pp. 823–834, 2015.
- [47] T. George Thuruthel, E. Falotico, M. Manti, A. Pratesi, M. Cianchetti, and C. Laschi, "Learning closed loop kinematic controllers for continuum manipulators in unstructured environments," *Soft robotics*, vol. 4, no. 3, pp. 285–296, 2017.
- [48] J. M. Bern, Y. Schnider, P. Banzet, N. Kumar, and S. Coros, "Soft robot control with a learned differentiable model," in *2020 3rd IEEE International Conference on Soft Robotics (RoboSoft)*. IEEE, 2020, pp. 417–423.
- [49] Z. Wang, T. Wang, B. Zhao, Y. He, Y. Hu, B. Li, P. Zhang, and M. Q.-H. Meng, "Hybrid adaptive control strategy for continuum surgical robot under external load," *IEEE Robotics and Automation Letters*, vol. 6, no. 2, pp. 1407–1414, 2021.
- [50] J. D. Ho, K.-H. Lee, W. L. Tang, K.-M. Hui, K. Althoefer, J. Lam, and K.-W. Kwok, "Localized online learning-based control of a soft redundant manipulator under variable loading," *Advanced Robotics*, vol. 32, no. 21, pp. 1168–1183, 2018.
- [51] G. Fang, X. Wang, K. Wang, K.-H. Lee, J. D. Ho, H.-C. Fu, D. K. C. Fu, and K.-W. Kwok, "Vision-based online learning kinematic control for soft robots using local gaussian process regression," *IEEE Robotics and Automation Letters*, vol. 4, no. 2, pp. 1194–1201, 2019.
- [52] T. G. Thuruthel, E. Falotico, F. Renda, and C. Laschi, "Model-based reinforcement learning for closed-loop dynamic control of soft robotic manipulators," *IEEE Transactions on Robotics*, vol. 35, no. 1, pp. 124–134, 2018.
- [53] X. You, Y. Zhang, X. Chen, X. Liu, Z. Wang, H. Jiang, and X. Chen, "Model-free control for soft manipulators based on reinforcement learning," in *2017 IEEE/RSJ International Conference on Intelligent Robots and Systems (IROS)*. IEEE, 2017, pp. 2909–2915.
- [54] Y. Ansari, M. Manti, E. Falotico, M. Cianchetti, and C. Laschi, "Multi-objective optimization for stiffness and position control in a soft robot arm module," *IEEE Robotics and Automation Letters*, vol. 3, no. 1, pp. 108–115, 2017.
- [55] S. Satheshbabu, N. K. Uppalapati, T. Fu, and G. Krishnan, "Continuous control of a soft continuum arm using deep reinforcement learning," in *2020 3rd IEEE International Conference on Soft Robotics (RoboSoft)*. IEEE, 2020, pp. 497–503.
- [56] H. Jiang, Z. Wang, Y. Jin, X. Chen, P. Li, Y. Gan, S. Lin, and X. Chen, "Hierarchical control of soft manipulators towards unstructured interactions," *The International Journal of Robotics Research*, vol. 40, no. 1, pp. 411–434, 2021.
- [57] Z. Q. Tang, H. L. Heung, K. Y. Tong, and Z. Li, "Model-based online learning and adaptive control for a "human-wearable soft robot" integrated system," *The International Journal of Robotics Research*, vol. 40, no. 1, pp. 256–276, 2021.
- [58] J. F. Queißer, K. Neumann, M. Rolf, R. F. Reinhart, and J. J. Steil, "An active compliant control mode for interaction with a pneumatic soft robot," in *2014 IEEE/RSJ International Conference on Intelligent Robots and Systems*. IEEE, 2014, pp. 573–579.
- [59] R. F. Reinhart, Z. Shareef, and J. J. Steil, "Hybrid analytical and data-driven modeling for feed-forward robot control," *Sensors*, vol. 17, no. 2, p. 311, 2017.
- [60] J.-J. E. Slotine and W. Li, "On the adaptive control of robot manipulators," *The international journal of robotics research*, vol. 6, no. 3, pp. 49–59, 1987.
- [61] J.-J. E. Slotine, W. Li *et al.*, *Applied nonlinear control*. Prentice hall Englewood Cliffs, NJ, 1991, vol. 199, no. 1.
- [62] A. Melingui, O. Lakhali, B. Daachi, J. B. Mbede, and R. Merzouki, "Adaptive neural network control of a compact bionic handling arm," *IEEE/ASME Transactions on Mechatronics*, vol. 20, no. 6, pp. 2862–2875, 2015.
- [63] F. L. Lewis, J. Campos, and R. Selmic, *Neuro-fuzzy control of industrial systems with actuator nonlinearities*. SIAM, 2002.
- [64] H. Dinh, S. Bhasin, and W. E. Dixon, "Dynamic neural network-based robust identification and control of a class of nonlinear systems," in *49th IEEE Conference on Decision and Control (CDC)*. IEEE, 2010.
- [65] S. Mbakop, G. Tagne, O. Lakhali, R. Merzouki, and S. V. Drakunov, "Path planning and control of mobile soft manipulators with obstacle avoidance," in *2020 3rd IEEE International Conference on Soft Robotics (RoboSoft)*. IEEE, 2020, pp. 64–69.
- [66] F. Xu, H. Wang, W. Chen, and Y. Miao, "Visual servoing of a cable-driven soft robot manipulator with shape feature," *IEEE Robotics and Automation Letters*, 2021.
- [67] E. Amanov, T.-D. Nguyen, and J. Burgner-Kahrs, "Tendon-driven continuum robots with extensible sections—a model-based evaluation of path-following motions," *The International Journal of Robotics Research*, vol. 40, no. 1, pp. 7–23, 2021.
- [68] J. Lai, B. Lu, Q. Zhao, and H. K. Chu, "Constrained motion planning of a cable-driven soft robot with compressible curvature modeling," *arXiv preprint arXiv:2106.08250*, 2021.
- [69] D. Navarro-Alarcon, H. M. Yip, Z. Wang, Y.-H. Liu, F. Zhong, T. Zhang, and P. Li, "Automatic 3-d manipulation of soft objects by robotic arms with an adaptive deformation model," *IEEE Transactions on Robotics*, vol. 32, no. 2, pp. 429–441, 2016.
- [70] D. Navarro-Alarcón, Y.-H. Liu, J. G. Romero, and P. Li, "Model-free visually servoed deformation control of elastic objects by robot manipulators," *IEEE Transactions on Robotics*, vol. 29, no. 6, pp. 1457–1468, 2013.
- [71] X. Li, X. Su, and Y.-H. Liu, "Vision-based robotic manipulation of flexible pcbs," *IEEE/ASME Transactions on Mechatronics*, vol. 23, no. 6, pp. 2739–2749, 2018.
- [72] M. Krstic, P. V. Kokotovic, and I. Kanellakopoulos, *Nonlinear and adaptive control design*. John Wiley & Sons, Inc., 1995.
- [73] D. Navarro-Alarcon, Y.-h. Liu, J. G. Romero, and P. Li, "On the visual deformation servoing of compliant objects: Uncalibrated control methods and experiments," *The International Journal of Robotics Research*, vol. 33, no. 11, pp. 1462–1480, 2014.
- [74] W. Chen, J. Zhou, S. S. Cheng, Y. Lu, F. Zhong, Y. Gao, Y. Wang, L. Xue, M. C. F. Tong, and Y.-H. Liu, "Tele-operated oropharyngeal swab (toos) robot enabled by tss soft hand for safe and effective sampling," *IEEE Transactions on Medical Robotics and Bionics*, 2021.
- [75] J. Zhou, Y. Chen, Y. Hu, Z. Wang, Y. Li, G. Gu, and Y. Liu, "Adaptive variable stiffness particle phalange for robust and durable robotic grasping," *Soft robotics*, vol. 7, no. 6, pp. 743–757, 2020.
- [76] K. He, X. Zhang, S. Ren, and J. Sun, "Delving deep into rectifiers: Surpassing human-level performance on imagenet classification," in *Proceedings of the IEEE international conference on computer vision*, 2015, pp. 1026–1034.